TU Delft

Delft University of Technology

Near-surface diffractor detection at archaeological sites based on an interferometric workflow

Liu, J.; Draganov, D.S.; Ghose, R.; Bourgeois, Q.

DOI
10.1190/GEO2020-0142.1

Publication date
2021

Document Version
Accepted author manuscript

Published in
Geophysics

Citation (APA)
Liu, J., Draganov, D. S., Ghose, R., & Bourgeois, Q. (2021). Near-surface diffractor detection at archaeological sites based on an interferometric workflow. *Geophysics*, *86*(3), WA1-WA11. https://doi.org/10.1190/GEO2020-0142.1

Important note
To cite this publication, please use the final published version (if applicable).
Please check the document version above.

Copyright
Other than for strictly personal use, it is not permitted to download, forward or distribute the text or part of it, without the consent of the author(s) and/or copyright holder(s), unless the work is under an open content license such as Creative Commons.

Takedown policy
Please contact us and provide details if you believe this document breaches copyrights.
We will remove access to the work immediately and investigate your claim.

This work is downloaded from Delft University of Technology.
For technical reasons the number of authors shown on this cover page is limited to a maximum of 10.

Near-surface diffractor detection at archaeological sites based on an interferometric workflow

Jianhuan Liu[1], Deyan Draganov[1], Ranajit Ghose[1] and Quentin Bourgeois[2]

[1]*Stevinweg 1, 2628 CN Delft,*

Department of Geoscience and Engineering,

Delft University of Technology

[2] *Einsteinweg 2, 2333 CC Leiden,*

Faculty of Archaeology,

Leiden University

(September 14, 2020)

GEO-2020-0142

Running head: ***Near-surface diffractor detection***

ABSTRACT

Detecting small-size objects is a primary challenge at archaeological sites due to the high degree of heterogeneity present in the near surface. Although high-resolution reflection seismic imaging often delivers the target resolution of the subsurface in different near-surface settings, the standard processing for obtaining an image of the subsurface is not suitable to map local diffractors. This happens because shallow seismic-reflection data are often dominated by strong surface waves which might cover weaker diffractions, and because traditional common-midpoint moveout corrections are only optimal for reflection events. Here, we propose an approach for imaging subsurface objects using masked diffractions. These masked diffractions are firstly revealed by a combination of seismic interferometry and non-

stationary adaptive subtraction, and then further enhanced through crosscoherence-based super-virtual interferometry. A diffraction image is then computed by a spatial summation of the revealed diffractions. We use phase-weighted stack to enhance the coherent summation of weak diffraction signals. Using synthetic data, we show that our scheme is robust in locating diffractors from data dominated by strong Love waves. We test our method on field data acquired at an archaeological site. The resulting distribution of shallow diffractors agrees with the location of anomalous objects identified in the V_S model obtained by elastic SH/Love full-waveform inversion using the same field data. The anomalous objects correspond to the position of a suspected burial, also detected in an independent magnetic survey and corings.

INTRODUCTION

Archaeology is the study of past human cultures through the analysis and interpretation of artifacts and material remains (Smith, 2014). The material remains, which possess certain physical properties (e.g., elastic impedance) that contrast with the subsurface background medium, can be detected by means of non-invasive near-surface geophysical surveys, and more specifically with the seismic methods. For detecting small, localized objects, the usual normal-moveout stacking is generally not useful, because traditional common-midpoint moveout corrections are only optimal for reflection events. Although common-offset gathers can potentially show such objects more reliably (Ghose et al., 1998), these gathers focus on the primary reflected waves and mostly ignore the diffracted waves. The conspicuous appearance of diffracted waves can be utilized to locate an object buried in the heterogeneous subsurface at an archaeological site. However, the amplitude of these diffracted events is usually weak (Klem-Musatov, 1994) and difficult to detect in field seismic data, due to the usually dominant presence of other coherent events like surface waves and specular reflections.

Several methods have been developed to detect various near-surface buried features using diffracted waves. Landa and Keydar (1998) develop an algorithm to construct a so-called diffraction-point-section (D-section) by concentrating the diffracted signals spread from diffractor points. In this D-section, high-amplitude anomalies indicate the existence of local heterogeneities. Shtivelman and Keydar (2005) present a multipath summation approach to stack diffracted signals along all possible diffraction trajectories for shallow inhomogeneities detection. Kaslilar et al. (2013) propose an approach inspired by seismic interferometry (SI) to estimate the location of a near-surface tunnel by traveltime inversion

of crosscorrelated diffracted arrivals. The crosscorrelation procedure eliminates the common raypath between the source and the subsurface diffractor. This makes the traveltime dependent only on properties between the receivers and the diffractors.

In this paper, we introduce a workflow for imaging subsurface objects using masked diffractions, i.e., weak diffractions covered by other signals. This workflow consists of three main steps. We first reveal masked diffractions by suppression of the dominant Love waves through a combination of SI and nonstationary adaptive subtraction (AS) (Dong et al., 2006; Halliday et al., 2007; Konstantaki et al., 2015; Liu et al., 2018). We then enhance the revealed weak diffraction signal through crosscoherence-based super-virtual interferometry (SVI) (Dai et al., 2011; Nakata et al., 2011; An and Hu, 2016; Place et al., 2019). Finally, a diffraction image, which can be used to interpret the locations of subsurface diffractors, is generated by a spatial summation (Shtivelman and Keydar, 2005; Landa et al., 2006; Shtivelman et al., 2009) of enhanced diffractions.

In the following, we first describe the theory of each of the above-mentioned steps. We then illustrate the feasibility of our approach in detecting near-surface objects using synthetic seismic data dominated by Love waves. Finally, we test our workflow on field seismic data acquired at an archaeological site in the Veluwe, the Netherlands, with the aim of mapping the distribution of shallow diffractors of archaeological importance.

METHODOLOGY

In this section, we present a workflow (Figure 1) for near-surface diffractor detection from data dominated by strong surface waves (in our case Love waves), which consists of three main steps. These steps include surface-waves suppression by SI+AS, diffraction enhance-

ment through SVI, and diffraction imaging. We list the full names of each acronyms used in this paper in Table 1. Below, we present the theory of each of these steps.

[Table 1 about here.]

[Figure 1 about here.]

SI+AS for surface-waves suppression

Seismic interferometry (SI) refers to a process of retrieving the seismic response between two receivers by crosscorrelating and integrating the wavefields recorded at these receivers from a boundary of sources (Wapenaar et al., 2008; Schuster, 2009). When the sources are located along the Earth's surface, the response retrieved by SI would be dominated by surface waves (Dong et al., 2006; Halliday et al., 2007). The dominance of surface waves is observed in passive seismology (Shapiro et al., 2005), exploration seismology (Dong et al., 2006; Balestrini et al., 2020), and near-surface seismology (Konstantaki et al., 2015). Depending on the source type (passive or active), the retrieval steps for SI are different. In the context of this paper, we focus only on active-source interferometry.

[Figure 2 about here.]

The steps of inter-receiver surface-wave retrieval using active sources are illustrated in Figure 2a. In Figure 2a, $\rightsquigarrow$ represents surface waves propagating along the Earth's surface from an active source to the receivers. By crosscorrelating the trace recorded at receiver $\mathbf{A}$ with that at $\mathbf{B}$, we obtain a virtual trace at $\mathbf{B}$ as if caused by a virtual source located at $\mathbf{A}$. The traveltime of this virtual trace is denoted as τ_{AB} (red $\rightsquigarrow$

in Figure 2a), and it is independent of the source position as long as the source falls inside the stationary-phase region (Snieder, 2004). For this reason, the virtual trace at **B** from each of the sources can be stacked constructively to give the inter-receiver estimate of the surface waves propagating from **A** to **B**. Mathematically, it can be formulated in the frequency domain as (Wapenaar and Fokkema, 2006; Halliday et al., 2007)

$$C_{X_B X_A} = \sum_{i=1}^{N} u(X_A, X_i) u^*(X_B, X_i). \tag{1}$$

In equation 1, $C_{X_B X_A}$ represents inter-receiver surface waves propagating from **A** to **B** retrieved by SI. The seismic data generated by a source at X_i and recorded by receiver at X_A and X_B are denoted as $u(X_A, X_i)$ and $u(X_B, X_i)$, respectively. The superscript $*$ indicates complex conjugation. N is the number of active sources available for stacking. If we ignore the presence of noise, in the frequency domain the seismic wavefield can also be represented by the multiplication of a source wavelet and a Green's function:

$$u(X, X_i) = W(X_i) G(X, X_i), \tag{2}$$

where $W(X_i)$ is the source wavelet generated by the source located at X_i and $G(X, X_i)$ denotes the Green's function between X_i and X. Substituting equation 2 into equation 1, we have

$$C_{X_B X_A} = W^2(X_i) \sum_{i=1}^{N} G(X_A, X_i) G^*(X_B, X_i). \tag{3}$$

To accurately retrieve the amplitude of the seismic response using equation 3, according to the theory, the sources should effectively surround the receivers and illuminate them homogeneously, the source boundary should be a sphere with sufficiently large radius, and the medium should be lossless (Draganov et al., 2006; Wapenaar and Fokkema, 2006). For conventional 2D near-surface seismic surveys, this requirement can not be fulfilled because active sources are placed only at the surface and usually along the line connecting the receivers (this limitation is also true for 2D seismic surveys at exploration scale); thus, the retrieved surface waves will be characterized by amplitude errors.

To account for the amplitude difference between the retrieved surface waves and the dominant surface waves from the physical active source, a matching filter (see Appendix A) is estimated via the regularized nonstationary regression technique proposed by Fomel (2009). This is done by using shaping regularization (Fomel, 2007) to constrain the continuity and smoothness of the filter coefficients. The retrieved surface waves are then convolved with this estimated matching filter and subsequently subtracted from the field data.

SVI for diffraction enhancement

After the suppression of the dominant surface waves, the hidden diffraction events may become identifiable. To further enhance the diffraction energy, we use a crosscoherence-based SVI (Dai et al., 2011). The principle of SVI consists of two steps and is illustrated in Figure 2b. First, the traces recorded at receivers **A** and **B** are crosscorrelated. The common raypath from source to a subsurface object (black straight line)

is subtracted, thus the traveltime of the obtained virtual diffraction can be denoted as $\tau_{OB} + \tau_{OA}$. This traveltime is the same for all active-source positions of a survey, so stacking the virtual diffraction at **B** from N sources will enhance its signal-to-noise ratio (S/N) by a factor of $\sqrt{N}$ assuming uncorrelated noise. Next, SI by convolution is applied (Slob et al., 2007) and the stacked virtual diffraction is convolved with an actual trace originally recorded at a receiver position **A** from the source at **X** to produce a super-virtual trace at **B**. This super-virtual trace represents the seismic response from a subsurface diffractor, recorded by receiver **B** from the source positioned at **X**. The super-virtual trace is kinematically equivalent (with traveltime equal to $\tau_{XO} + \tau_{OB}$) for all receiver positions **A** located between the source **X** and receiver **B**. Thus, the retrieved super-virtual traces at N receiver positions **A** could be stacked to obtain a final trace with S/N increased again by as much as $O(\sqrt{N})$.

In this paper, we use crosscoherence instead of crosscorrelation (similar to equation 1) to retrieve the virtual diffraction $H_{X_B X_A}$ (Nakata et al., 2011; Place et al., 2019):

$$H_{X_B X_A} = \sum_{i=1}^{N} \frac{u(X_A, X_i) u^*(X_B, X_i)}{|u(X_A, X_i)||u^*(x_B, X_i)| + \eta} = \sum_{i=1}^{N} \frac{G(X_A, X_i) G^*(X_B, X_i)}{|G(X_A, X_i)||G^*(x_B, X_i)| + \eta}, \quad (4)$$

where η is a small number for stabilizing the division, and $|\cdot|$ indicates that the amplitude spectrum is used. If we consider the effect of the source wavelet, which is denoted by $W(X_i)$, a virtual diffraction obtained by crosscorrelation will contain an amplitude factor proportional to $W^2(X_i)$ (see equation 3). The corresponding super-virtual diffraction will then include an amplitude factor proportional to $W^3(X_i)$, due

to the additional convolution involved in the second step. This $W^3(X_i)$ factor may lead to wavelet distortion of the enhanced diffractions. On the other hand, SI by crosscoherence (equation 4) eliminates (theoretically) the contribution of the source wavelet $W(X_i)$ and makes the virtual diffraction contain only the medium response. The resulting super-virtual diffraction will then contain an amplitude factor proportional to $W(X_i)$, which avoids wavelet distortion and thus improves the precision of the reconstructed diffractions.

Diffraction imaging

The diffractions that are revealed by SI+AS and enhanced by SVI can now be used for detecting near-surface diffractors. We design a diffraction algorithm (based on studies from Landa and Keydar (1998) and Shtivelman and Keydar (2005)) to coherently focus the diffraction energy back to its original position; all other events in the shot-gather domain will be suppressed by the used directional summation. Such procedure will make the true diffractions appear as high-amplitude anomalies in the resulting sections, which can be used to indicate the locations of diffractors.

Consider a seismic wave emitted from a source X_0 (Figure 3). When it encounters a subsurface diffractor along its propagation path, it would generate a secondary wave that spreads from this point in all directions. In Figure 3, X_i is the image point and Ω denotes the diffracted wavefront element surrounding this image point. We assume that the velocity variations are small and the propagation distance between source and receiver is relatively short, so that the diffracted wavefronts can be approximated as an arc of a circle with a radius of R. This radius R has a specific physical meaning,

which is the depth of the diffractor below the image point. Thus, the kinematic response (T_{sr}) of the diffractor recorded by receivers can be written as (Landa and Keydar, 1998)

[Figure 3 about here.]

$$T_{sr} = \frac{\sqrt{(X_0 - X_i)^2 + R^2} + \sqrt{(X_k - X_i)^2 + R^2}}{V_0} - \frac{2R}{V_0} + 2t_d, \tag{5}$$

where V_0 is the average velocity of the medium above the diffractor, t_d is the vertical time above the diffractor. X_0, X_i, X_k denote the lateral positions of the source (s), image point, and receiver (r), respectively.

If we know the exact value of R (the depth of the diffractor), a diffraction image can be obtained by stacking seismic energy along the diffraction surface defined by equation 5. If the value of R is unknown, it can be estimated by maximizing the semblance function (Taner and Koehler, 1969) calculated from seismic records within a time window along the traveltime surface defined by equation 5 (similar to the traditional velocity analysis). The alternative approach for diffraction imaging, not requiring the specification of the radius R, is the multipath summation (Shtivelman and Keydar, 2005; Shtivelman et al., 2009). This is done by stacking seismic energy (with unit weights) along diffraction trajectories defined by equation 5, calculated for various values of R within a specified range. The resulting diffraction image would be close to the one produced by stacking with the correct radius, due to the constructive and destructive interference of the amplitudes contributing along each diffraction trajectory.

The practical implementation steps of this diffraction-stacking method include the following. For a specific common-source gather, we first assume that the diffractor is located directly under the first receiver and the depth of the diffractor is known as R. This will define a specific diffraction traveltime curve according to equation 5. Next, we obtain a diffraction-moveout corrected gather by applying diffraction-moveout correction to this common-source gather. Such a traveltime correction is repeated for all other combinations of source-receiver pairs. We then resort these moveout-corrected common-source gathers into the common-receiver domain and stack traces within each common-receiver gather to produce one single trace per receiver position. To enhance coherent summation of weak diffraction signals, a phase-weighted stack (PWS) (see Appendix B) method is used. The stacked traces from each common-receiver gather are then assembled into a diffraction image (Landa and Keydar, 1998; Liu et al., 2019). For better visualization of high-amplitude anomalies, we produce the final diffraction image using a coherency measure calculated from each diffraction image resulting from different R. The coherency measure we choose is the unnormalized crosscorrelation sum (Neidell and Taner, 1971), due to its high sensitivity to coherent weak signals. This coherency function (C) can be expressed as

$$C = \sum_{t} \left\{ \Big[\sum_{i=1}^{M} f_{i,t(i)} \Big]^2 \right\}, \tag{6}$$

where $f_{i,t(i)}$ denotes the amplitude value of the ith trace at two-way traveltime $t(i)$, and M is the number of traces. The outer summation is performed over the two-way zero-offset time samples t within a time gate. The length of the gate should be approximately equal to the main wavelength of the seismic signal.

SYNTHETIC TEST

To verify the effectiveness of our method for near-surface diffractor detection, we first test it on data from 2D synthetic modeling. The model shown in Figure 4 is an S-wave velocity (V_S) model. This model consists of two layers. The first layer has a lower velocity (100 m/s) and thickness of 0.5 m. Below this layer, we place a high-velocity (150 m/s) half-space. Two circular diffractors are also embedded in the model at a depth of 5 m. These diffractors have a certain impedance contrast with respect to the background medium. The size of these diffractors is 1.0 m. The receiver array, which is located at the surface, consists of 40 geophones aligned in the horizontal direction from 10 m to 29.5 m at an interval of 0.5 m. During data generation, the receiver array is kept fixed, while the source, also deployed at the surface, advances at a step of 1 m. The first source is located 5 m to the left of the first geophone, while the last source is placed 4.5 m to the right of the last geophone. With this acquisition geometry, 30 common-source gathers are computed using an elastic 2D SH finite-difference algorithm (Bohlen, 2002; Dokter et al., 2017). We discuss the reason for choosing SH-wave processing in the field-example section. At the top boundary, a free-surface boundary condition is realised by the image technique (Robertsson, 1996) for accurate SH-wave modeling. For the other boundaries, convolutional perfectly matched layers (CPML) absorbing boundary conditions are used (Komatitsch and Martin, 2007). The source signature is a band-limited spike with the central frequency at 40 Hz.

[Figure 4 about here.]

Revealing weak diffractions

Figure 5a shows an example of the synthetic shot gathers for the source located at horizontal position 13 m, i.e., at the seventh receiver. This shot gather (Figure 5a) is dominated by dispersive Love waves, because the presence of the high-velocity half-space in the velocity model. The amplitudes of the diffracted waves in Figure 5a, which represent the seismic response from the diffractors embedded in the model in Figure 4, are so weak that it is difficult to identify them directly.

Before we introduce our SI+AS scheme for the suppression of Love waves, we first apply conventional frequency-wavenumber ($f-k$) filtering to eliminate the dominant Love waves, while preserving the weak diffraction signals. Figure 6a displays the $f-k$ spectrum of the synthetic gather from Figure 5a. We can see that this spectrum is dominated by two clusters of Love-wave energy (black arrows). We design a fan filter to reject the Love-wave energy in the $f-k$ domain (Figure 6b). This is followed by inverse mapping back to the shot-gather domain. As shown in the resulting filtered shot gather (Figure 7a), weak diffraction signals begin to be identifiable, due to the significant suppression of the Love waves. However, we can still observe some remaining Love waves (red box in Figure 7a). This is because Love waves and diffractions are not well separated in the $f-k$ domain (Figure 6a) due to their similar apparent velocities. Thus, it is hard to design an efficient fan filter, which can completely reject the Love-wave energy while preserving the diffraction events.

We then make use of SI to compute a virtual common-source gather for the receiver positioned at 13 m (this receiver becomes the virtual source), following the scheme

presented in Figure 2a. As shown in Figure 5b, the main kinematic characteristics of the Love waves in Figure 5a are retrieved well. However, due to the source term $W^2(X_i)$ involved in the SI procedure (equation 3), the wavelet of the Love waves in Figure 5b is broader then that in Figure 5a. Further, the interferometric approximation used in equation 3, such as elastic media and active sources distributed only at the surface, causes the amplitude of the estimated Love waves in Figure 5b to be erroneous compared to the amplitude of the Love waves in the original shot gather in Figure 5a.

To account for amplitude, phase, and frequency differences between Figure 5a and Figure 5b, a matching filter is estimated via the regularized nonstationary regression technique proposed by Fomel (2007). Figure 5d shows the mean coefficients of the matching filter determined by minimizing the difference between Figure 5a and Figure 5b in the least-squares sense. From Figure 5d, we can see that the filter coefficients vary in both time and space, which agrees well with the variability of the original shot gather (Figure 5a). We then convolve the estimated matching filter (Figure 5d) with Figure 5b to compensate for the amplitude, phase, and frequency distortions in Figure 5b that we mentioned earlier, which leads to the result presented in Figure 5c. Comparing Figure 5a with Figure 5c, we can now see that the dominant Love waves in Figure 5c and Figure 5a match very well. Next, we subtract Figure 5c from Figure 5a, which gives the result shown in Figure 7b. As shown in Figure 7b, two diffraction events with negative moveouts can now be easily recognized. This is due to the significant suppression of Love waves in Figure 5a through the SI + AS procedure (Figure 2a).

During the procedure of AS, the dominant Love waves dictate the parameters of the matching filter, and hence these waves will be most effectively suppressed. The weak diffraction signals might also be affected, but to a lesser extent. As shown in Figure 7b, certain parts of diffractions which overlap with the Love wave are also regarded as Love-wave energy by this algorithm (Figure 2a) and suppressed. To recover this lost diffraction energy and further enhance the amplitude of the diffraction events, we then apply SVI to the data as in Figure 7b, obtaining results as shown in Figure 7c. For comparison, we also show, a reference shot gather (Figure 7d) containing only the seismic response from the diffractors. This shot gather is obtained by taking the difference of synthetic data modeled with and without the diffractors. This process removes any arrivals other than the diffractions. Comparing Figure 7c with Figure 7b, we can see that the diffractions in Figure 7c show more complete moveouts (see blue boxes in Figure 7b and 7c), and their apices are recovered well.

[Figure 5 about here.]

[Figure 6 about here.]

[Figure 7 about here.]

Diffraction imaging

We now apply our diffraction-focusing approach to the data shown in Figure 7, i.e., after the suppression of the Love waves by different approaches, which gives the corresponding diffraction images (Figure 8). In this figure, the horizontal axes show

the lateral location (in m) as shown in Figure 4, while the vertical axes denote the approximate depth (in m) that we derive using an average velocity ($V_0 = 150$ m/s) from the model in Figure 4. We also use this average velocity ($V_0 = 150$ m/s) in equation 5 to describe the moveouts of possible diffractions. The range of R (depth of potential diffractors) used for diffraction stacking is from 0.5 m to 8 m with a step of 0.5 m. Such a range covers the area of interest for near-surface diffractor detection. To mitigate the near-field effects as much as possible, we mute early arrivals before producing the final diffraction images.

Figures 8a–8c represent the diffraction images from the data after Love-wave elimination by the $f - k$ filtering, SI+AS, and SI+AS+SVI, respectively. Every second common-source gathers is used. We apply PWS to enhance the coherent summation of weak signals. From Figures 8a–8c, we can clearly identify two prominent anomalies (red color). We interpret the maximum amplitudes of these anomalies as the centers of the detected diffractors, whose lateral locations agree well with those of the objects embedded in the synthetic model (Figure 4). There are some errors in the estimated depths of the detected diffractors (around 6 m). This can be explained by the fact that a constant velocity ($V_0 = 150$ m/s) may not be accurate enough to describe the travel path of diffracted waves and hence may cause errors in the estimated depths. Note that the shapes of the anomalies in Figures 8a–8c do not necessarily indicate the actual shapes of the true objects in Figure 4. Figures 8d–8f show diffraction images as in Figures 8a–8c, respectively, but using all modeled common-source gathers. We show this result to investigate the effect of the number of common-source gathers on the resolution of the diffraction images. We can see that having half as many

sources did not affect the resolution of the obtained diffraction images. This is very encouraging for field applications, where due to operational reasons sparser source points would be available. In the field data example below, we have sources every 2 m. Figures 8g–8i show diffraction images as in Figures 8d–8f, respectively, but using linear stack for weak diffraction summations. We can see that the resolution of the anomalies in Figures 8d–8f is higher than in Figures 8g–8i. This is because PWS is more efficient for incoherent-noise reduction than linear stack, thus reducing the amount of incoherent noise present in the resulting diffraction image.

[Figure 8 about here.]

FIELD EXAMPLE

Site overview

In 2017, we acquired seismic data at the Epe-Niersen barrow alignment, an archaeological site located in the Veluwe, the Netherlands. With our survey, we wanted to obtain more information about such monuments (burial mounds) using non-invasive geophysical methods, including seismic imaging, with the aim to minimize or even completely eliminate the need for excavation. To do that, we investigated one burial mound from the Epe-Niersen barrow alignment, which is known as Mound 4749 (Bourgeois, 2012).

Seismic-data acquisition

We carried out a seismic survey over the top of Mound 4749. We used two kinds of active sources — a sledge-hammer and a high-frequency S-wave vibrator (Ghose et al., 1996; Brouwer et al., 1997) — to excite seismic waves recorded by horizontal, 10-Hz single-component geophones. The horizontal geophones were oriented in the crossline direction, while the active sources (hammer and vibrator) were used in the SH mode, i.e., also oriented in the crossline direction. Under such acquisition system, we can generate and record SH-wave.

We used SH-waves because they have several main advantages over P- and/or SV-waves. The first advantage is that they can offer higher resolution of subsurface structures then P/SV-waves, given the same frequency content. This is due to the relatively low propagation velocity of SH-wave in soft soils and ensuing wavelength. The second benefit of SH-waves is that they are directly linked to the small-strain rigidity and hence quite sensitive to subtle changes in the subsoil mechanical properties (Ghose, 2003; Ghose and Goudswaard, 2004; Ghose et al., 2013). Another advantage is that when SH-waves encounter a diffractive object in the subsurface, the diffracted wavefield will mainly consist of SH-wave diffractions. For P/SV-waves, however, such discontinuity will cause a complex diffracted wavefield, which includes P-P, P-SV, SV-P and SV-SV diffractions. Of all these diffraction modes, the SH-wave diffractions have the largest amplitude and most coherent phase characteristic along the traveltime hyperbola, making it advantageous for diffraction imaging (Lellouch and Reshef, 2017; Peterie et al., 2020). Our receiver array consists of 120 geophones planted with a 0.25 m interval. During data acquisition, we kept this receiver array

fixed and moved only the source at an interval of 2 m. The first source position was at 4 m to the left of the first geophone, while the last source position was at 4 m to the right of the last geophone. At each source position, four recordings were acquired and stacked to yield one common-source gather. This was done to reduce the source-incoherent noise and increase the S/N of the recorded data.

Near-surface diffractors detection

Figure 9a shows a typical raw SH-wave common-source gather when using the sledge-hammer source, in this case at lateral position of 0 m. Figure 9b shows an example shot gather when using the vibrator as source at the same source position, after crosscorrelation of the raw vibrograms with the estimated groundforce (Ghose, 2002). The main preprocessing steps that we apply to these two types of seismic data are trace editing, top muting, statics corrections, geometrical-spreading correction, trace normalization, and band-pass filtering ($5 - 80$ Hz). Due to the soft-soil condition in the near surface of our study area, we can see that the raw seismograms (Figure 9a and Figure 9b) are dominated by distinct, dispersive Love waves. The strong presence of these Love waves makes it hard to identify the diffraction events, if they exist, directly from the raw data. To reveal possible weak diffracted energy, these dominant Love waves have to be suppressed while the diffraction events should also be preserved.

[Figure 9 about here.]

To attenuate the Love waves, we first retrieve the dominant Love-wave energy from the preprocessed data by SI in a data-driven way, as explained above, and then

adaptively subtract the retrieved result from the raw data (Figure 9a and 9b), i.e., we apply SI+AS which leads to the results shown in Figure 9c and 9d, respectively. Comparing the latter with the respective gathers illustrated in Figure 9a and 9b, some meaningful diffraction events caused by heterogeneities in the subsurface (e.g., red circles in Figure 9c and 9d) can be identified. To further enhance these diffracted events and suppress other coherent signals, we then apply SVI to the data as shown in Figure 9c and 9d. The results are shown in Figure 9e and 9f, respectively. As in the synthetic example (Figure 6), Love waves and masked diffraction signals in the preprocessed data (Figure 9a and 9b) map to the similar regions in the $f-k$ domain. In such cases, it is hard to design an efficient filter to suppress the Love waves and preserve the weak diffractions at the same time. Because of this fact, we choose not to apply conventional $f-k$ filtering to suppress Love waves in the field data.

Figure 10 illustrates the four final diffraction images obtained from the hammer and vibrator datasets (after SI+AS, SI+AS+SVI) using our diffraction-focusing approach described in the Methodology section. The average velocity that we use for diffraction stacking is 90 m/s. We base this velocity value on the results from an iterative full-waveform inversion (FWI) algorithm (Tarantola, 1984; Virieux and Operto, 2009). Note that the diffraction-focusing approach does not require detailed subsurface information, but assumes a homogeneous value characteristic of the velocity close to the surface (V_0 in equation 5). This assumptions is only valid at sites with gradual velocity variation. Figure 11 shows the inverted V_S model by elastic SH/Love FWI using the hammer data. From the velocity model (Figure 11) obtained by FWI, we think that here the near-surface (< 1.0 m) is quite homogeneous laterally

and can be, on average, described by a single velocity ($V_0 = 90$ m/s). We stack the diffraction events in the shot domain over diffractor depths from 0.5 m to 5.0 m (R in equation 5), which mainly covers the depth range of our interest in the shallow subsurface. In Figure 10, the horizontal axes show lateral locations of the receiver array that we deployed over the Mound 4749, while the vertical axes indicate the approximate depth (in m) converted from time using an average velocity of 90 m/s.

Figure 10a and 10c display diffraction images obtained from sledge-hammer and S-wave vibrator data after Love-wave suppression by SI+AS. Figure 10b and 10d represent diffraction images from sledge-hammer and S-wave vibrator data after Love-wave suppression by SI+AS and diffraction enhancement by SVI. Two clusters of high-amplitude anomalies (indicated by ellipses) can be identified at similar positions (around 15 m and 22 m horizontal distance) in these four diffractions images. From the V_S model (Figure 11) obtained by FWI, we can see that areas at similar positions also show high-velocity (blue ellipses) contrasts with the background medium. These facts give us more confidence to interpret these distinct anomalies (ellipses in Figure 10) as potential buried objects of archaeological importance.

In an earlier separate field work, a magnetic survey was conducted at this site (Lambers et al., 2017). This survey detected magnetic anomalies in the range of $\pm 5 \sim 8$ nT, which is nearly the strongest value among their measurements made within the mound. The configuration of the anomalies and their position within the burial mound suggest these are probably traces of a burial underneath the mound. Additional corings also confirm the place of a pit at this position — most likely a grave. Earlier excavations of burial mounds in the direct vicinity of this mound

have found evidence for large stones that were incorporated within the structure of the graves (Bourgeois et al., 2009). The high-amplitude anomalies detected in our diffraction images (Figure 10) might correspond to such stones.

During a seismic survey, when seismic waves encounter such stones, the waves would be diffracted due to the strong impedance contrast of the stones with the background medium. In the shot gathers after SI+AS and SI+AS+SVI, we can identify diffraction events (red circles in Figure 9), with apices located at around 15 m horizontal distance. However, the diffraction event at around 22 m horizontal distance is not recognizable in the shot gathers. A possible explanation is that the S/N of this diffraction is still low in them. However, after coherent summation of this weak diffraction in the following diffraction-stacking procedure, its amplitude becomes strong enough and can be easily identified in the final diffraction images (dashed ellipses in Figure 10). Comparing the diffraction images from data after SI+AS and SI+AS+SVI, we can see that the high-amplitude anomalies in SI+AS+SVI diffraction image (ellipses in Figure 10b and 10d) seem to be more easily identifiable than those in the SI+AS diffraction image (ellipses in Figure 10a and 10c).

[Figure 10 about here.]

[Figure 11 about here.]

DISCUSSION

When a propagating seismic wave encounters a subsurface object or a velocity perturbation of size comparable to the wavelength, it will be diffracted. For a 2D seismic

survey, the imaging of the target objects is reliable only when the seismic data are acquired along a line above such targets. If this is not the case, the imaging of diffractors will be negatively affected (spatially smeared or estimated at a wrong location).

In the modeled example, we saw that $f-k$ filtering could damage the desired diffraction arrivals. In our case, it indeed resulted in such a damage to the right sides of the diffractions (Figure 7a). Still, the energy at and around the apices of the diffractions was preserved, and the diffraction stacking gave good results, possibly even better than the results from our proposed methodology. Figure 7b (and the filter in Figure 5d) show that SI+AS had damaged the diffraction apices with the result of less strong diffraction stacking. The application of SVI partly compensated for that and thus the diffraction stacking produced better results. Note that this is also a result of the modeling, as the diffractions are relatively strong and thus the SI step retrieves not only the dominant Love waves, but also the apices of the diffractions. In the case of the field data, the diffraction events are not clear at all. In such cases, the damaging effect of the $f-k$ filter on diffraction events, which map into the same region in the $f-k$ domain as the Love-wave energy, would lead to a lower diffraction-stacking image. Contrary to this, our proposed methodology, making use of a data-driven Love-wave suppression and diffraction-event enhancement through SI+AS+SVI, would not result in damaging but in enhancement, and thus would produce better diffraction-stacking image.

The two datasets corresponding to two different seismic sources, sledge-hammer and S-wave vibrator, used in this study were independently acquired and processed. The horizontal locations of diffractors are well-constrained by surface seismic meth-

ods (Peterie et al., 2020). The very close lateral locations of the diffractors derived from the diffraction focusing applied on SI+AS and SI+AS+SVI processed datasets (Figure 10) validate our interpretation regarding the presence of these diffractors and their approximate lateral locations. The estimated depths of the detected diffractors have inherent uncertainty and are connected to the average velocity V_0 in equation 5. Assuming a constant velocity may not be enough to describe the travel path of the diffracted waves, especially at sites with strong lateral or vertical velocity variations. This may contribute to errors in the estimated depths. The estimated depth information of the detected diffractors could be verified by other geophysical method (such as core profiling) once their horizontal locations are determined.

After Love-wave suppression and diffraction enhancement, diffraction events (red ellipses in Figure 9) with clear apices could be identified. These diffraction events are representative of subsurface heterogeneities, and are useful to map the distribution of buried objects at an archaeological site. However, as mentioned above, a diffraction image can only indicate the approximate location of the subsurface objects. To obtain a more complete picture regarding the subsurface objects of archaeological importance, use of 3D seismic imaging and near-surface FWI could be important options, which is the direction of our future research.

CONCLUSION

We present a workflow for imaging shallow subsurface objects represented by weak diffractions hidden behind dominant surface waves (in our case Love waves). Our workflow includes three main steps. The masked diffractions are first revealed after

the suppression of the dominant Love waves. This is done by retrieving the Love waves in a data-driven way by seismic interferometry and then adaptively subtracting them from the raw data. Secondly, we enhance the revealed weak diffraction signals further through crosscoherence-based super-virtual interferometry. Thirdly, we produce a diffraction section by a spatial summation of the revealed diffraction energy, where no specific velocity for the subsurface is needed. We introduce phase-weighted stack to enhance the coherent summation of weak diffraction signals. Using synthetic data, we illustrate that our workflow is robust in detecting and imaging weak diffractions. We apply our workflow on seismic datasets acquired in an archaeological site using two different active seismic sources. Our results show two prominent diffraction objects in the subsurface at our test location. Our workflow has the potential to be used to map the spatial locations of shallow heterogeneities in near-surface seismic surveys, when no detailed subsurface velocity is available.

ACKNOWLEDGMENTS

The first author is sponsored by the China Scholarship Council (File No. 201604910851). We thank Dominique Ngan-Tillard for the help during the field data acquisition. The authors would like to thank the associate editor Ariel Lellouch and four anonymous reviewers for their constructive comments that have significantly improved the manuscript.

APPENDIX A

NON-STATIONARY MATCHING FILTER ESTIMATION

Matched filtering is a method to measure time-varying differences between two signals (Fomel, 2009). In this paper, we use it for the adaptive subtraction of surface waves. Consider two time series — prediction $\mathbf{p}(t)$ and observation $\mathbf{b}(t)$. A stationary matching filter $\mathbf{f}(\gamma)$ can obtained by stretching $\mathbf{p}(t)$ to different scales in order to match $\mathbf{p}(t)$ and $\mathbf{d}(t)$. This can be formalized as the following least-squares inversion problem:

$$\min \Big| \sum_{\gamma} \mathbf{p}(\gamma t) * \mathbf{f}(\gamma) - \mathbf{d}(t) \Big|^2, \tag{A-1}$$

where $*$ denotes the convolution operator, γ is a stretching variable. For a particular value of the stretching variable γ, equation A-1 gives a single measurement $\mathbf{f}(\gamma)$ for all the time coordinates. To handle the inherent non-stationary seismic data, a time-varying matching filter $\mathbf{f}(\gamma, t)$ is needed. As equation A-1 shows, this $\mathbf{f}(\gamma, t)$ can be obtained by minimizing the following objective function:

$$\min \Big| \sum_{\gamma} \mathbf{p}(\gamma t) * \mathbf{f}(\gamma, t) - \mathbf{d}(t) \Big|^2. \tag{A-2}$$

Equation A-2 is an ill-posed problem because it contains more unknown variables than constraints. One remedy is to add additional constraints, i.e., regularization, to constrain the variability of the filter coefficients. With shaping regularization (Fomel, 2007), equation A-2 can be solved as

$$\mathbf{f}(\gamma,t)=\left[\lambda^2\mathbf{I}+\mathbf{S}\left(\mathbf{P}^T\mathbf{P}-\lambda^2\mathbf{I}\right)\right]^{-1}\mathbf{S}\mathbf{P}^T\mathbf{d}, \tag{A-3}$$

where λ is a scaling coefficient , which is defined as $\lambda=|\mathbf{p}(t)|^2$. $\mathbf{P}$ is the data matrix composed of $\mathbf{p}(\gamma t)$. $\mathbf{S}$ denotes the shaping operator, which is chosen as a triangle smoothing operator in this paper.

APPENDIX B

PHASE-WEIGHTED STACK METHOD

Phase-weighted stack (PWS) is a technology first proposed by Schimmel and Paulssen (1997) to detect weak but coherent arrivals. The basic idea underlying PWS is to suppress components of stacked signals, which do not share the same instantaneous phase. Following the notations from Schimmel and Paulssen (1997), a complex trace $S(t)$ is constructed from a seismic trace $s(t)$ and its Hilbert transform $\mathcal{H}[s(t)]$:

$$S(t)=s(t)+i\mathcal{H}(s(t)), \tag{B-1}$$

which can also be expressed by amplitude $A(t)$ and instantaneous phase $\Phi(t)$:

$$S(t)=A(t)exp[i\Phi(t)], \tag{B-2}$$

where

$$A(t)=\sqrt{s^2(t)+\mathcal{H}^2(s(t))}, \tag{B-3}$$

and

$$\Phi(t) = \arctan \frac{\mathcal{H}(s(t))}{s(t)}. \tag{B-4}$$

Schimmel and Paulssen (1997) define the following **phase stack** $c(t)$, where no amplitudes of complex traces are explicitly involved:

$$c(t) = \frac{1}{N} \Big| \sum_{j=1}^{N} exp[i\phi_j(t)] \Big|, \tag{B-5}$$

where N is the number of traces involved in stacking, j is the index of each trace. The amplitude of the phase stack $c(t)$ varies between 0 and 1, as schematically illustrated by Figure B-1. As shown in Figure B-1a, the amplitude of the phase stack $c(t)$ equals 1, if the instantaneous phase of the two traces are exactly the same (coherent) at time t. On the other hand, when the instantaneous phase of the two traces varies quite significantly, $c(t)$ will be approximately 0 (Figure B-1b). Thus, we can use the phase stack to weight the summation of all the traces — $g(t)$ is expressed as

[Figure B-1 about here.]

$$g(t) = \frac{[c(t)]^{\nu}}{N} \sum_{j=1}^{N} s_j(t). \tag{B-6}$$

In equation B-6, $[c(t)]^{\nu}$ is used to enhance coherent signals, that is, signals with similar phase. The exponent ν controls the transition between more coherent and less incoherent signal summations. In our paper, we use $\nu = 2$, as suggested by Schimmel and Paulssen (1997). When ν equals 0, equation B-6 reduces to the conventional, linear stack.

REFERENCES

An, S., and T. Hu, 2016, Suppression of seismic surface waves based on adaptive weighted super-virtual interferometry: Science China Earth Sciences, **59**, 2179–2188.

Balestrini, F., D. Draganov, A. Malehmir, P. Marsden, and R. Ghose, 2020, Improved target illumination at ludvika mines of sweden through seismic-interferometric surface-wave suppression: Geophysical Prospecting, **68**, 200–213.

Bohlen, T., 2002, Parallel 3-D viscoelastic finite difference seismic modelling: Computers & Geosciences, **28**, 887–899.

Bourgeois, Q., 2012, Monuments on the horizon: the formation of the barrow landscape throughout the 3rd and 2nd millennium BC: Sidestone Press.

Bourgeois, Q., L. Amkreutz, and R. Panhuysen, 2009, The niersen beaker burial: A renewed study of a century-old excavation: Journal of Archaeology in the Low Countries, **1**, 83–105.

Brouwer, J., R. Ghose, K. Helbig, and V. Nijhof, 1997, The improvement of geotechnical subsurface models through the application of s-wave reflection seismic exploration: 3rd Annual Meeting, EEGS, Extended Abstracts, 103–106.

Dai, W., T. Fei, Y. Luo, and G. T. Schuster, 2011, Super-virtual interferometric diffractions as guide stars: 81th Annual International Meeting, SEG, Expanded Abstracts, 3819–3823.

Dokter, E., D. Köhn, D. Wilken, D. De Nil, and W. Rabbel, 2017, Full waveform inversion of SH-and Love-wave data in near-surface prospecting: Geophysical Prospecting, **65**, 216–236.

Dong, S., R. He, and G. T. Schuster, 2006, Interferometric prediction and least squares subtraction of surface waves: 76th Annual International Meeting, SEG, Expanded Abstracts, 2783–2786.

Draganov, D., K. Wapenaar, and J. Thorbecke, 2006, Seismic interferometry: Reconstructing the earth's reflection response: Geophysics, **71**, no. 4, SI61–SI70.

Fomel, S., 2007, Shaping regularization in geophysical-estimation problems: Geophysics, **72**, no. 2, R29–R36.

———, 2009, Adaptive multiple subtraction using regularized nonstationary regression: Geophysics, **74**, no. 1, V25–V33.

Ghose, R., 2002, High-frequency shear wave reflections from shallow subsoil layers using a vibrator source: Sweep cross-correlation versus deconvolution with ground-force derivative: 72th Annual International Meeting, SEG, Expanded Abstracts, 1408–1411.

———, 2003, High-frequency shear-wave reflections to monitor lateral variations in soil, supplementing downhole geotechnical tests: *in* J. Saveur, ed., Reclaiming the underground space: Swets & Zeitlinger, 827–833.

Ghose, R., J. Brouwer, and V. Nijhof, 1996, A portable S-wave vibrator for high-resolution imaging of the shallow subsurface: 58nd Annual International Conference and Exhibition, EAGE, Extended Abstracts, M037.

Ghose, R., J. Carvalho, and A. Loureiro, 2013, Signature of fault zone deformation in near-surface soil visible in shear wave seismic reflections: Geophysical Research Letters, **40**, 1074–1078.

Ghose, R., and J. Goudswaard, 2004, Integrating S-wave seismic-reflection data and

cone penetration test data using a multiangle multiscale approach: Geophysics, **69**, 440–459.

Ghose, R., V. Nijhof, J. Brouwer, Y. Matsubara, Y. Kaida, and T. Takahashi, 1998, Shallow to very shallow, high-resolution reflection seismic using a portable vibrator system: Geophysics, **63**, 1295–1309.

Halliday, D. F., A. Curtis, J. O. Robertsson, and D.-J. van Manen, 2007, Interferometric surface-wave isolation and removal: Geophysics, **72**, no. 5, A69–A73.

Kaslilar, A., U. Harmankaya, K. Wapenaar, and D. Draganov, 2013, Estimating the location of a tunnel using correlation and inversion of rayleigh wave scattering: Geophysical Research Letters, **40**, 6084–6088.

Klem-Musatov, K., 1994, Theory of seismic diffractions: Society of Exploration Geophysicists.

Komatitsch, D., and R. Martin, 2007, An unsplit convolutional perfectly matched layer improved at grazing incidence for the seismic wave equation: Geophysics, **72**, no. 5, SM155–SM167.

Konstantaki, L., D. Draganov, R. Ghose, and T. Heimovaara, 2015, Seismic interferometry as a tool for improved imaging of the heterogeneities in the body of a landfill: Journal of Applied Geophysics, **122**, 28–39.

Lambers, L., J. W. E. Fassbinder, K. Lambers, and Q. Bourgeois, 2017, The iron-age burial mounds of epe-nierson, the Netherlands: results from magnetometry in the range of ± 1.0 nT: 12th International Conference of Archaeological Prospection, 132–134.

Landa, E., S. Fomel, and T. Moser, 2006, Path-integral seismic imaging: Geophysical

Prospecting, **54**, 491–503.

Landa, E., and S. Keydar, 1998, Seismic monitoring of diffraction images for detection of local heterogeneities: Geophysics, **63**, 1093–1100.

Lellouch, A., and M. Reshef, 2017, Shallow diffraction imaging in an sh-wave crosshole configurationcrosshole sh diffraction imaging: Geophysics, **82**, no. 1, S9–S18.

Liu, J., Q. Bourgeois, R. Ghose, and D. Draganov, 2019, Detection of near-surface heterogeneities at archaeological sites using seismic diffractions: First Break, **37**, 93–97.

Liu, J., D. Draganov, and R. Ghose, 2018, Seismic interferometry facilitating the imaging of shallow shear-wave reflections hidden beneath surface waves: Near Surface Geophysics, **16**, 372–382.

Nakata, N., R. Snieder, T. Tsuji, K. Larner, and T. Matsuoka, 2011, Shear wave imaging from traffic noise using seismic interferometry by cross-coherence: Geophysics, **76**, no. 6, SA97–SA106.

Neidell, N. S., and M. T. Taner, 1971, Semblance and other coherency measures for multichannel data: Geophysics, **36**, 482–497.

Peterie, S. L., R. D. Miller, J. Ivanov, and S. D. Sloan, 2020, Shallow tunnel detection using sh-wave diffraction imaging: Geophysics, **85**, no. 2, EN29–EN37.

Place, J., D. Draganov, A. Malehmir, C. Juhlin, and C. Wijns, 2019, Crosscoherence-based interferometry for the retrieval of first arrivals and subsequent tomographic imaging of differential weathering: Geophysics, **84**, no. 4, Q37–Q48.

Robertsson, J. O., 1996, A numerical free-surface condition for elastic/viscoelastic finite-difference modeling in the presence of topography: Geophysics, **61**, 1921–

1934.

Schimmel, M., and H. Paulssen, 1997, Noise reduction and detection of weak, coherent signals through phase-weighted stacks: Geophysical Journal International, **130**, 497–505.

Schuster, G. T., 2009, Seismic interferometry: Cambridge University Press.

Shapiro, N. M., M. Campillo, L. Stehly, and M. H. Ritzwoller, 2005, High-resolution surface-wave tomography from ambient seismic noise: Science, **307**, 1615–1618.

Shtivelman, V., and S. Keydar, 2005, Imaging shallow subsurface inhomogeneities by 3d multipath diffraction summation: First Break, **23**, 39–42.

Shtivelman, V., S. Keydar, and M. Mikenberg, 2009, Imaging near-surface inhomogeneities using weighted multipath summation: Near Surface Geophysics, **7**, 171–177.

Slob, E., D. Draganov, and K. Wapenaar, 2007, Interferometric electromagnetic green's functions representations using propagation invariants: Geophysical Journal International, **169**, 60–80.

Smith, C., 2014, Encyclopedia of global archaeology: Springer Reference.

Snieder, R., 2004, Extracting the green's function from the correlation of coda waves: A derivation based on stationary phase: Physical Review E, **69**, 046610.

Taner, M. T., and F. Koehler, 1969, Velocity spectra-digital computer derivation applications of velocity functions: Geophysics, **34**, 859–881.

Tarantola, A., 1984, Inversion of seismic reflection data in the acoustic approximation: Geophysics, **49**, 1259–1266.

Virieux, J., and S. Operto, 2009, An overview of full-waveform inversion in exploration

geophysics: Geophysics, **74**, no. 6, WCC1–WCC26.

Wapenaar, K., D. Draganov, and J. O. Robertsson, 2008, Seismic interferometry: History and present status: Society of Exploration Geophysicists.

Wapenaar, K., and J. Fokkema, 2006, Green's function representations for seismic interferometry: Geophysics, **71**, no. 4, SI33–SI46.

LIST OF FIGURES

1 Flowchart for raw-data processing for diffraction imaging. To reveal weak diffractions, a combination of seismic interferometry (SI) and adaptive subtraction (AS) is firstly used to suppress dominating surface waves (SW). A crosscoherence-based super-virtual interferometry (SVI) is then applied to further enhance the diffractions. . . . . .

2 (a) The step for retrieving dominant surface waves between two receivers by SI. (b1), (b2) The steps for creating super-virtual diffractions with an increased signal-to-noise ratio (S/N). Note that the surface-wave component can also be retrieved/enhanced by the SVI step. Hence, it is beneficial to apply SVI for diffraction enhancement only after suppression of the dominant surface waves. $\bigotimes$, $\bigodot$, $\bigoplus$ denote crosscorrelation-, crosscoherence-, and crossconvolution-based operators, respectively. $\rightsquigarrow$ represents surface waves propagating along the surface from an active source to the receivers. $\rightarrow$ denotes the propagation of diffracted waves from an active source to the receivers. . . . . .

3 Schematic view of diffracted waves. X_0, X_i, X_k denote the lateral position of the source (red star), image point (blue triangle), and receiver (black triangle), respectively. Ω is the diffracted wavefront element surrounding the image point (blue triangle at lateral position X_i). . . . . .

4 S-wave velocity (V_S) model used to generate the synthetic common-source gathers. Two shallow diffractors with a given impedance contrast with respect to the background media are included in the model. . . . . .

5 Steps for revealing weak diffractions dominated by strong Love waves. (a) A synthetic SH shot gather computed for the model shown in Figure 4; (b) retrieved Love waves from the gather as shown in Figure 5a; (c) result after convolution of the data in (b) with the matching filter (d); (d) mean filter coefficients estimated by minimizing the difference between (a) and (b), using the regularized non-stationary regression method. . . . . .

6 (a) The frequency-wavenumber ($f-k$) spectrum of the synthetic SH shot gather from Figure 5a; (b) the $f-k$ spectrum of the same shot gather, but after rejecting Love-wave energy indicated by the black arrows in (a). . . .

7 (a) Result after Love-wave suppression in the data in Figure 5a by $f-k$ filtering; (b) result after adaptive subtraction of Figure 5b from Figure 5a; (c) result after applying SVI to the result in (b) for diffraction enhancement; (d) reference shot gather showing only diffracted arrivals obtained from subtraction of modeled data using models with and without diffractors. . . . .

8 Comparison of results from diffraction imaging by different approaches. (a),(b),(c) diffraction imaging of the data after Love-wave suppression by $f-k$ filtering, SI+AS, and SI+AS+SVI, respectively. Every second common-source gather is used. Phase-weighted stack (PWS) is applied to enhance the coherent summation of weak diffraction signals. (d),(e),(f) Similar to (a), (b), (c), but using all the modeled common-source gathers. (g), (h), (i) Similar to (d), (e), (f), but ordinary, linear stack is used to stack the weak diffraction signals.

9 (a) A typical preprocessed SH-wave shot gather from the field data acquired using a sledge-hammer source. The gather is dominated by strong Love waves. (c) Result after Love-wave suppression by SI+AS; (e) result after diffraction enhancement by SVI; (b),(d),(f) are the same as (a),(c),(e), but using S-wave vibrator as the source. The first 101 traces are displayed. . . .

10 Diffraction imaging result obtained from the field seismic data following our proposed workflow 1: (a) sledge-hammer data after Love-wave suppression by SI+AS; (b) sledge-hammer data after Love-wave suppression by SI+AS and diffraction enhancement by SVI; (c), (d) are same as (a), (b) but using S-wave vibrator data. High-amplitude anomalies (solid and dashed ellipses) indicate the potential locations of subsurface diffractor-like objects. . . . .

11 Two-dimensional subsurface V_S model obtained by elastic full-waveform inversion of the sledge-hammer data. . . . . .

B-1 Illustrations of the summation of $exp[i\phi_1(t)]$ and $exp[i\phi_2(t)]$ in the complex plane. Red arrows denote these two vectors, while the blue vector is the addition of these two vectors. (a) When two signals have the same instantaneous phase ($\phi_1(t) = \phi_2(t)$), the amplitude of the phase sum (blue arrow) will be 2, and the corresponding value of $c(t)$ will be 1. (b) When two signals have significantly different instantaneous phases, the amplitude of the phase sum (blue arrow) and the corresponding value of $c(t)$ will be approximately 0. Modified from Schimmel and Paulssen (1997). . . . . .

LIST OF TABLES

1 A list of acronyms used in this paper. . . . . .

Acronyms	Full names
AS	Adaptive subtraction
F-K	Frequency-wavenumber
FWI	Full-waveform inversion
PWS	Phase-weighted stack
SI	Seisimc interferometry
SVI	Super-virtual interferometry

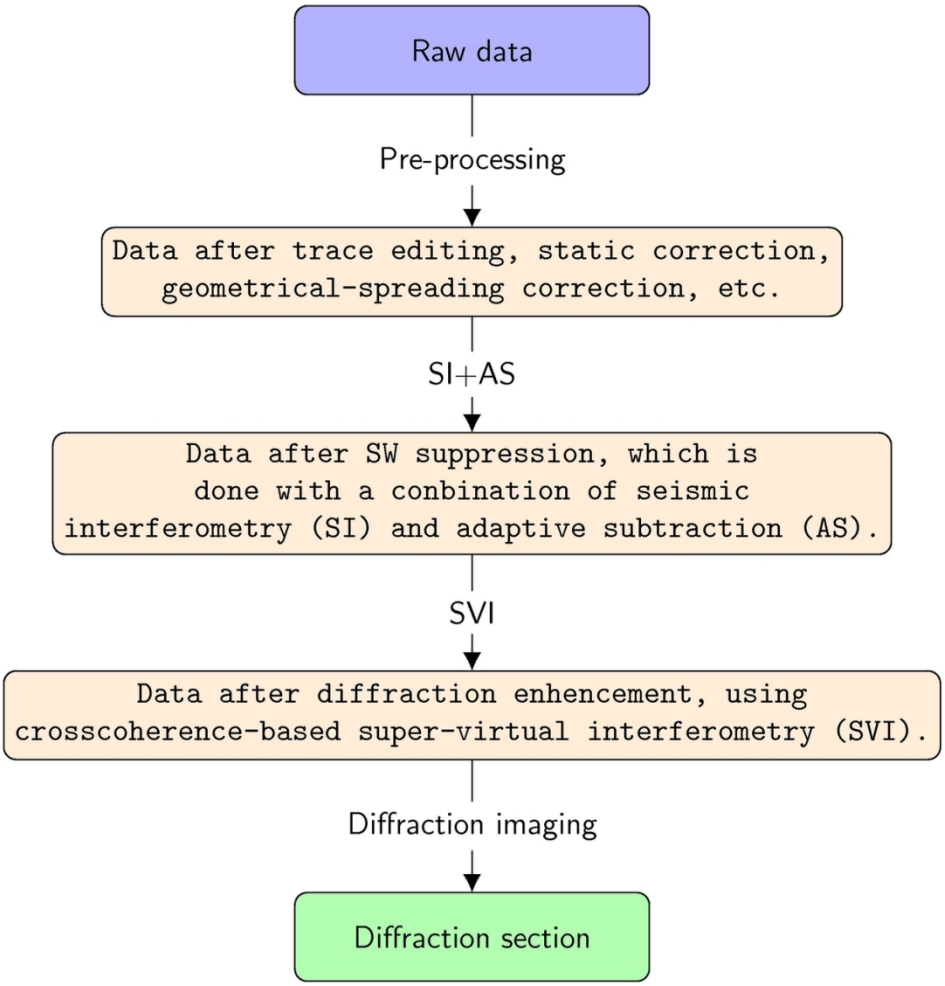


Figure 1: Flowchart for raw-data processing for diffraction imaging. To reveal weak diffractions, a combination of seismic interferometry (SI) and adaptive subtraction (AS) is firstly used to suppress dominating surface waves (SW). A crosscoherence-based super-virtual interferometry (SVI) is then applied to further enhance the diffractions.

112x117mm (300 x 300 DPI)

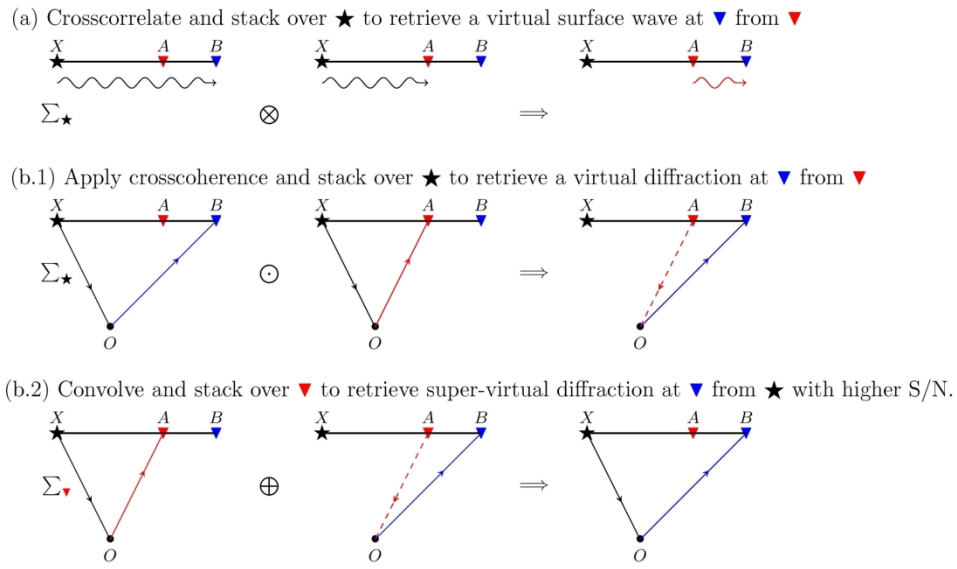


Figure 2: (a) The step for retrieving dominant surface waves between two receivers by SI. (b1), (b2) The steps for creating super-virtual diffractions with an increased signal-to-noise ratio (S/N). Note that the surface-wave component can also be retrieved/enhanced by the SVI step. Hence, it is beneficial to apply SVI for diffraction enhancement only after suppression of the dominant surface waves. $\bigotimes$, $\bigodot$, $\bigoplus$ denote crosscorrelation-, crosscoherence-, and crossconvolution-based operators, respectively. $\leadsto$ represents surface waves propagating along the surface from an active source to the receivers. $\to$ denotes the propagation of diffracted waves from an active source to the receivers.

188x113mm (300 x 300 DPI)

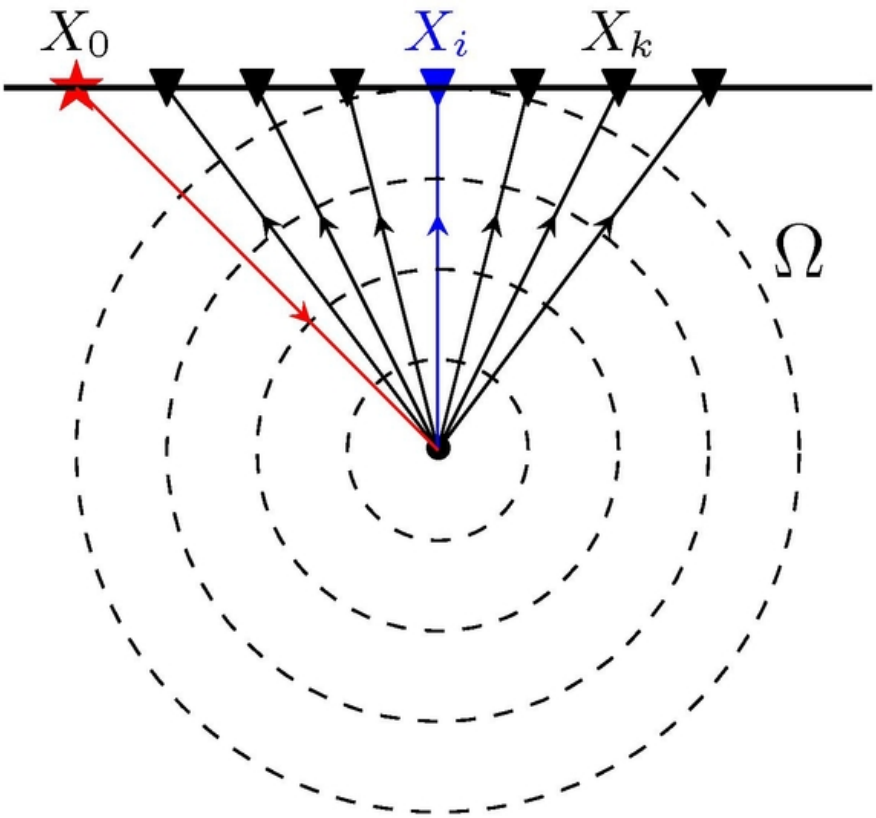


Figure 3: Schematic view of diffracted waves. X_0, X_i, X_k denote the lateral position of the source (red star), image point (blue triangle), and receiver (black triangle), respectively. Ω is the diffracted wavefront element surrounding the image point (blue triangle at lateral position X_i).

55x52mm (300 x 300 DPI)

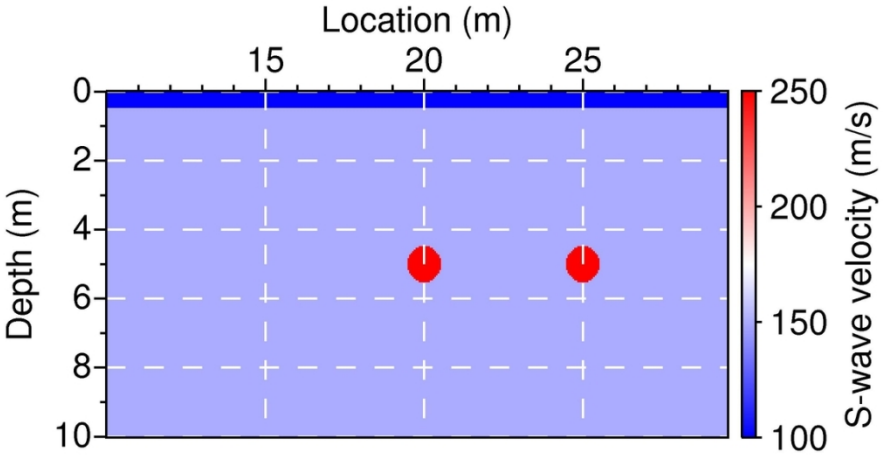


Figure 4: S-wave velocity (V_S) model used to generate the synthetic common-source gathers. Two shallow diffractors with a given impedance contrast with respect to the background media are included in the model.

110x67mm (300 x 300 DPI)

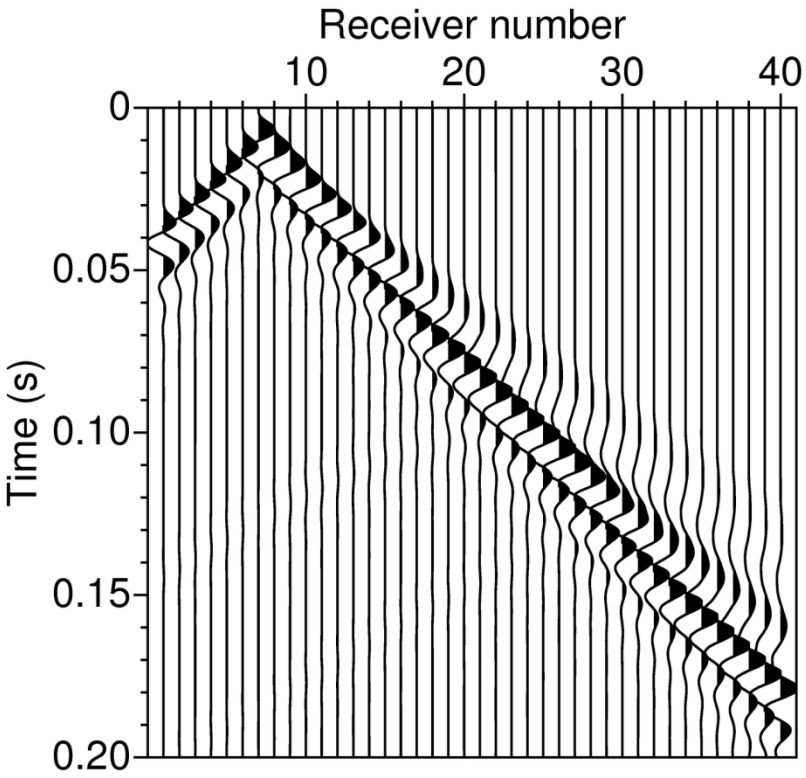


Figure 5a: Steps for revealing weak diffractions dominated by strong Love waves. (a) A synthetic SH shot gather computed for the model shown in Figure 4; (b) retrieved Love waves from the gather as shown in Figure 5a; (c) result after convolution of the data in (b) with the matching filter (d); (d) mean filter coefficients estimated by minimizing the difference between (a) and (b), using the regularized non-stationary regression method.

156x150mm (300 x 300 DPI)

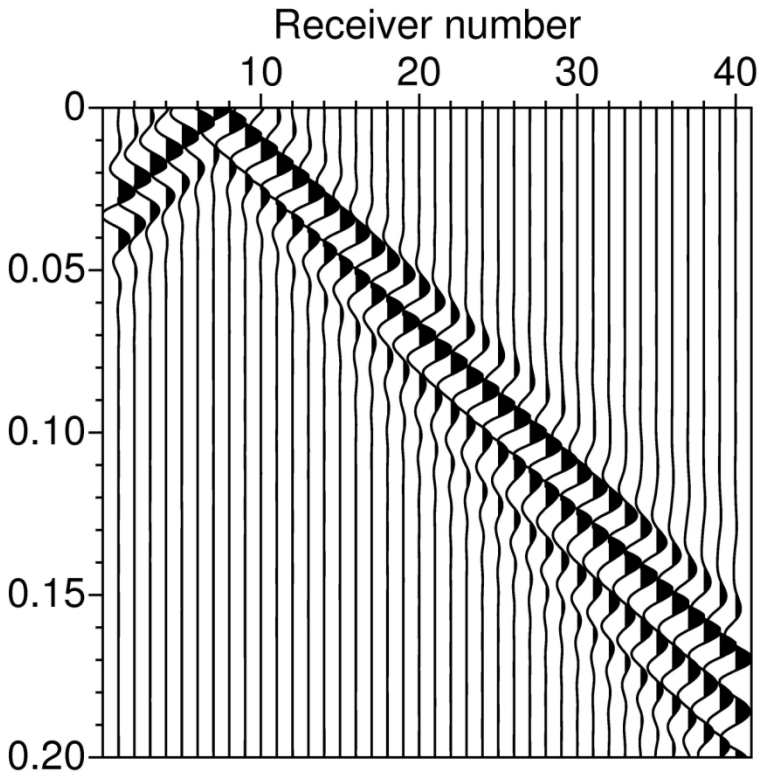


Figure 5b: Steps for revealing weak diffractions dominated by strong Love waves. (a) A synthetic SH shot gather computed for the model shown in Figure 4; (b) retrieved Love waves from the gather as shown in Figure 5a; (c) result after convolution of the data in (b) with the matching filter (d); (d) mean filter coefficients estimated by minimizing the difference between (a) and (b), using the regularized non-stationary regression method.

156x150mm (300 x 300 DPI)

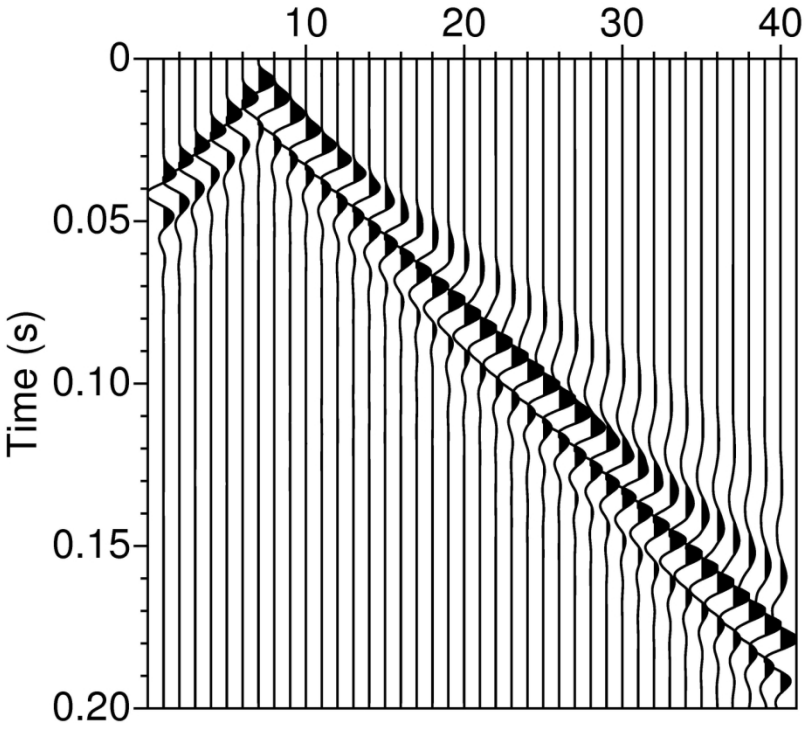


Figure 5c: Steps for revealing weak diffractions dominated by strong Love waves. (a) A synthetic SH shot gather computed for the model shown in Figure 4; (b) retrieved Love waves from the gather as shown in Figure 5a; (c) result after convolution of the data in (b) with the matching filter (d); (d) mean filter coefficients estimated by minimizing the difference between (a) and (b), using the regularized non-stationary regression method.

156x150mm (300 x 300 DPI)

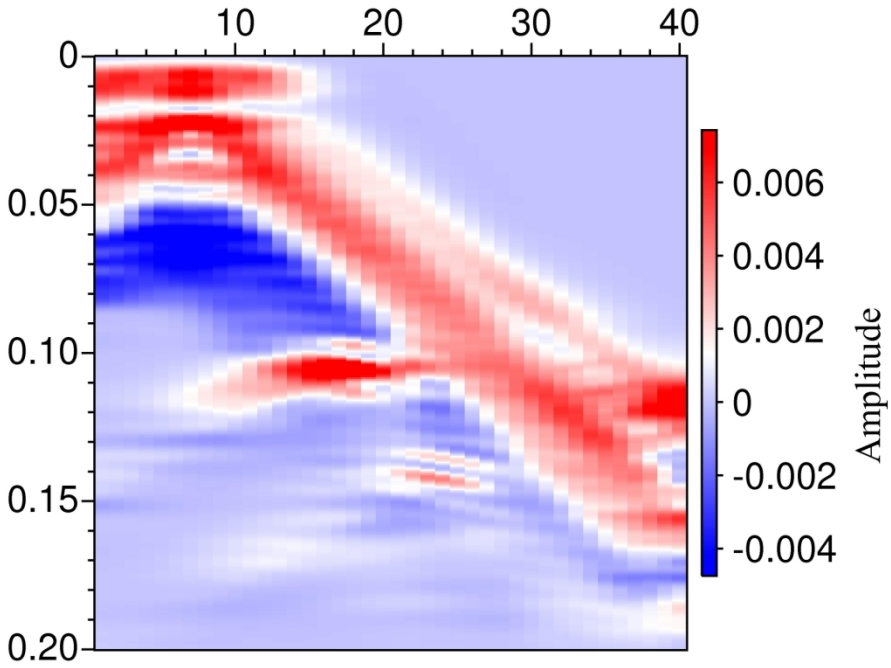


Figure 5d: Steps for revealing weak diffractions dominated by strong Love waves. (a) A synthetic SH shot gather computed for the model shown in Figure 4; (b) retrieved Love waves from the gather as shown in Figure 5a; (c) result after convolution of the data in (b) with the matching filter (d); (d) mean filter coefficients estimated by minimizing the difference between (a) and (b), using the regularized non-stationary regression method.

171x150mm (300 x 300 DPI)

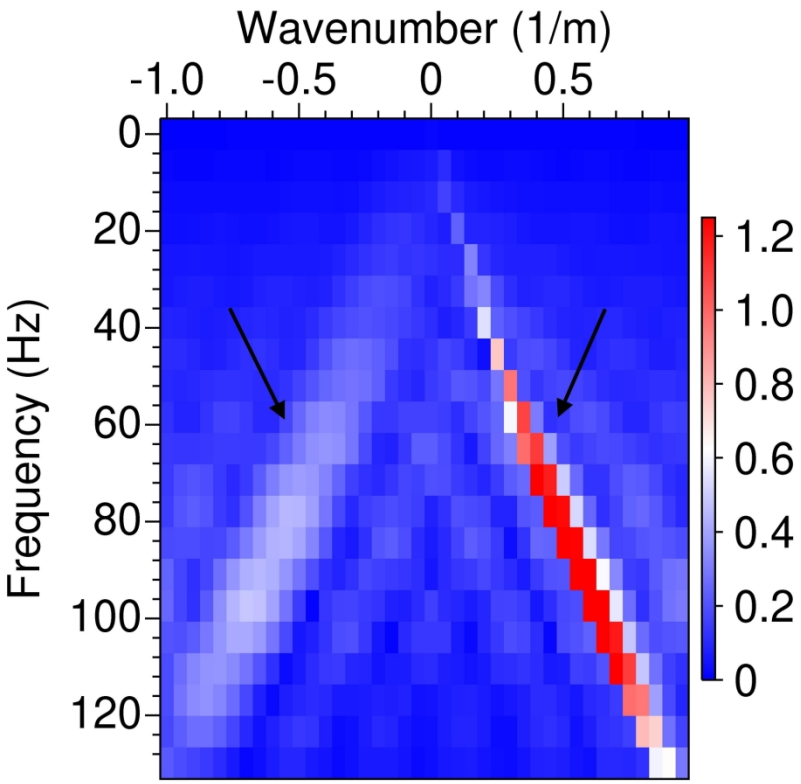


Figure 6a: (a) The frequency-wavenumber ($f-k$) spectrum of the synthetic SH shot gather from Figure 5a; (b) the $f-k$ spectrum of the same shot gather, but after rejecting Love-wave energy indicated by the black arrows in (a).

192x185mm (300 x 300 DPI)

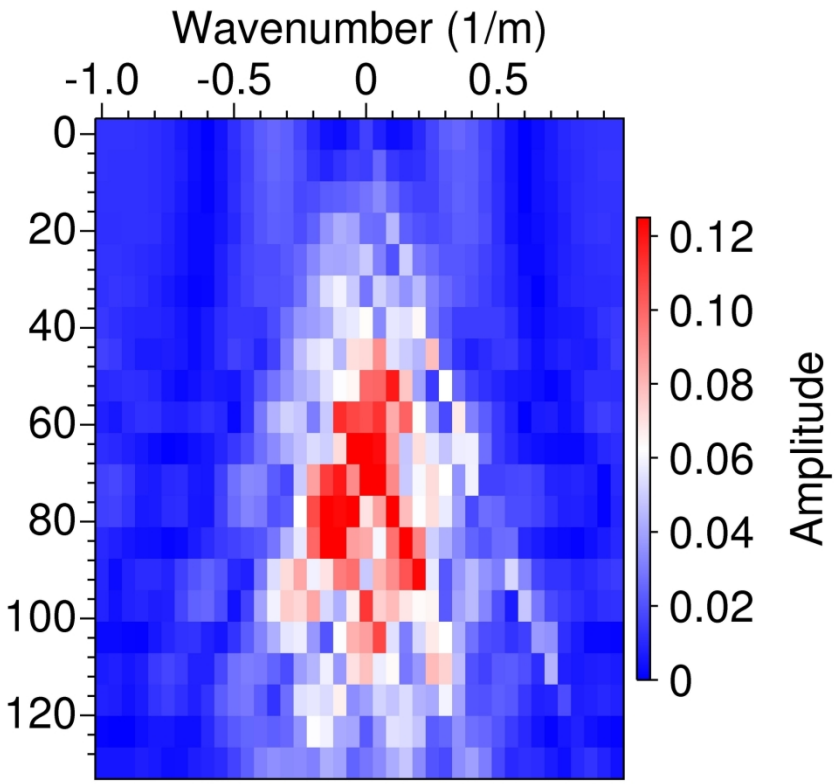


Figure 6b: (a) The frequency-wavenumber ($f-k$) spectrum of the synthetic SH shot gather from Figure 5a; (b) the $f-k$ spectrum of the same shot gather, but after rejecting Love-wave energy indicated by the black arrows in (a).

192x185mm (300 x 300 DPI)

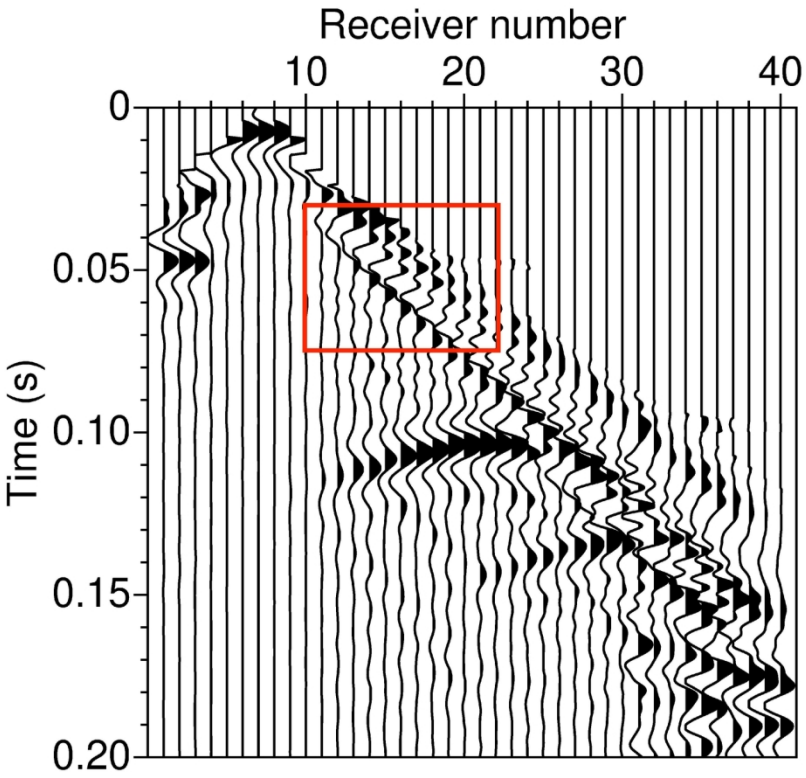


Figure 7a: (a) Result after Love-wave suppression in the data in Figure 5a by $f-k$ filtering; (b) result after adaptive subtraction of Figure 5b from Figure 5a; (c) result after applying SVI to the result in (b) for diffraction enhancement; (d) reference shot gather showing only diffracted arrivals obtained from subtraction of modeled data using models with and without diffractors.

156x150mm (300 x 300 DPI)

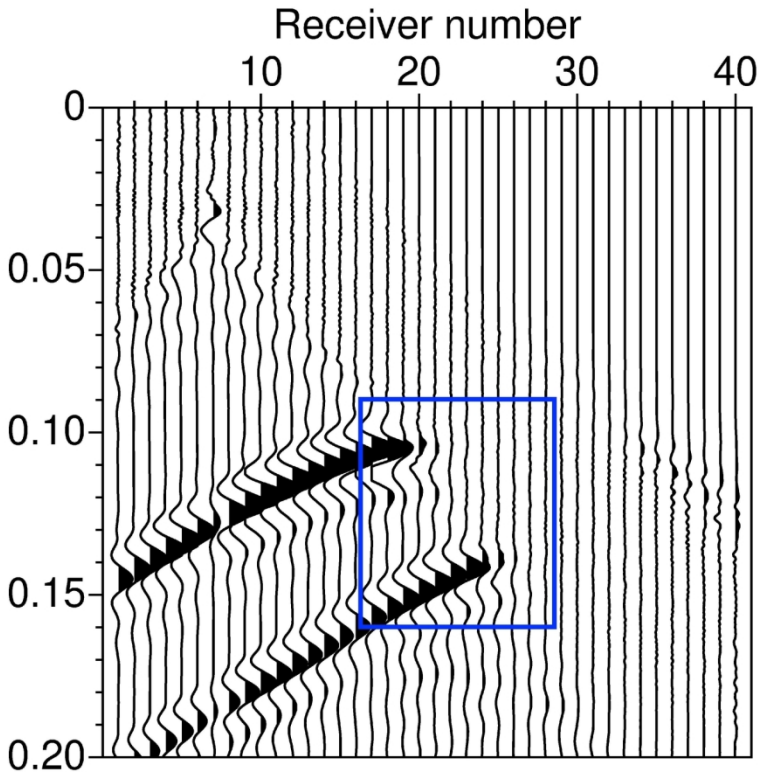


Figure 7b: (a) Result after Love-wave suppression in the data in Figure 5a by $f-k$ filtering; (b) result after adaptive subtraction of Figure 5b from Figure 5a; (c) result after applying SVI to the result in (b) for diffraction enhancement; (d) reference shot gather showing only diffracted arrivals obtained from subtraction of modeled data using models with and without diffractors.

156x150mm (300 x 300 DPI)

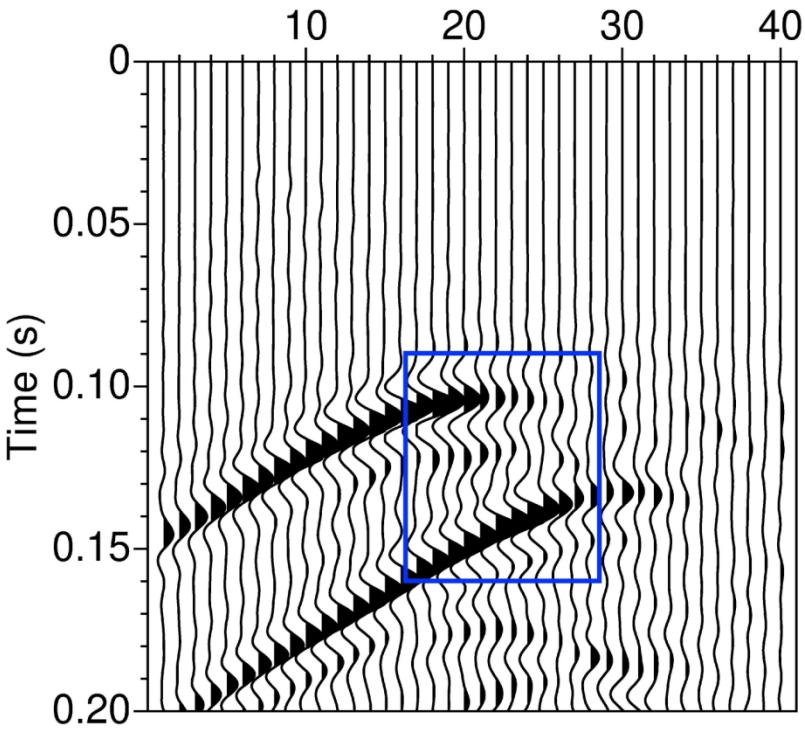


Figure 7c: (a) Result after Love-wave suppression in the data in Figure 5a by $f-k$ filtering; (b) result after adaptive subtraction of Figure 5b from Figure 5a; (c) result after applying SVI to the result in (b) for diffraction enhancement; (d) reference shot gather showing only diffracted arrivals obtained from subtraction of modeled data using models with and without diffractors.

156x150mm (300 x 300 DPI)

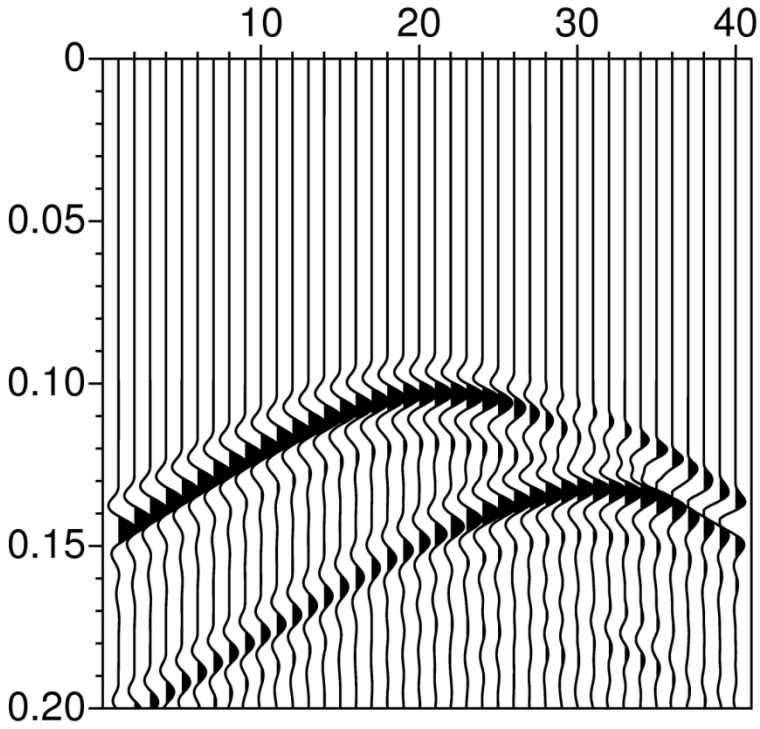


Figure 7d: (a) Result after Love-wave suppression in the data in Figure 5a by $f-k$ filtering; (b) result after adaptive subtraction of Figure 5b from Figure 5a; (c) result after applying SVI to the result in (b) for diffraction enhancement; (d) reference shot gather showing only diffracted arrivals obtained from subtraction of modeled data using models with and without diffractors.

156x150mm (300 x 300 DPI)

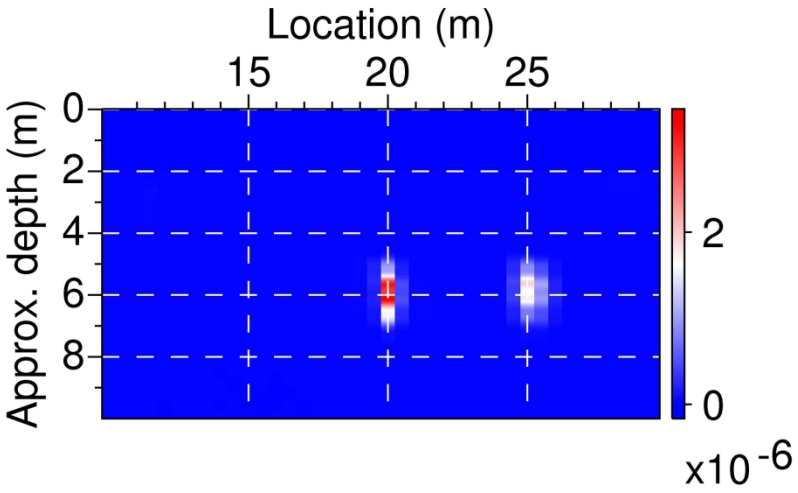


Figure 8a: Comparison of results from diffraction imaging by different approaches. (a),(b),(c) diffraction imaging of the data after Love-wave suppression by $f-k$ filtering, SI+AS, and SI+AS+SVI, respectively. Every second common-source gather is used. Phase-weighted stack (PWS) is applied to enhance the coherent summation of weak diffraction signals. (d),(e),(f) Similar to (a), (b), (c), but using all the modeled common-source gathers. (g), (h), (i) Similar to (d), (e), (f), but ordinary, linear stack is used to stack the weak diffraction signals.

204x122mm (300 x 300 DPI)

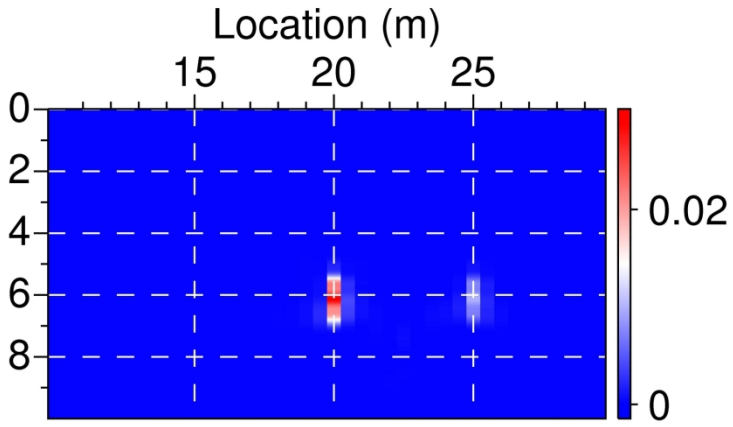


Figure 8b: Comparison of results from diffraction imaging by different approaches. (a),(b),(c) diffraction imaging of the data after Love-wave suppression by $f-k$ filtering, SI+AS, and SI+AS+SVI, respectively. Every second common-source gather is used. Phase-weighted stack (PWS) is applied to enhance the coherent summation of weak diffraction signals. (d),(e),(f) Similar to (a), (b), (c), but using all the modeled common-source gathers. (g), (h), (i) Similar to (d), (e), (f), but ordinary, linear stack is used to stack the weak diffraction signals.

204x122mm (300 x 300 DPI)

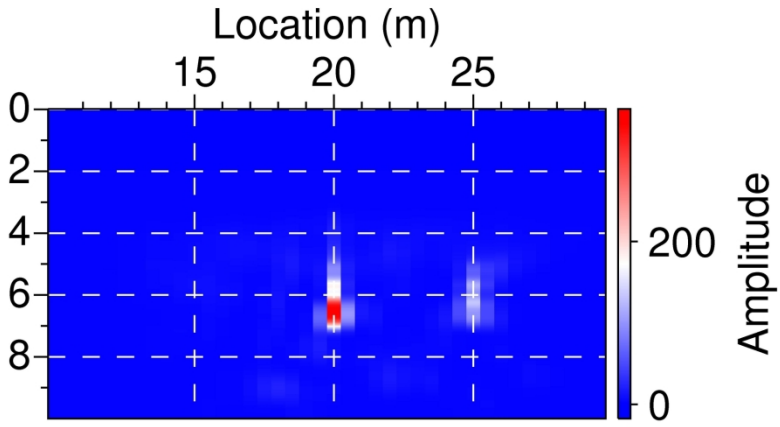


Figure 8c: Comparison of results from diffraction imaging by different approaches. (a),(b),(c) diffraction imaging of the data after Love-wave suppression by $f-k$ filtering, SI+AS, and SI+AS+SVI, respectively. Every second common-source gather is used. Phase-weighted stack (PWS) is applied to enhance the coherent summation of weak diffraction signals. (d),(e),(f) Similar to (a), (b), (c), but using all the modeled common-source gathers. (g), (h), (i) Similar to (d), (e), (f), but ordinary, linear stack is used to stack the weak diffraction signals.

204x122mm (300 x 300 DPI)

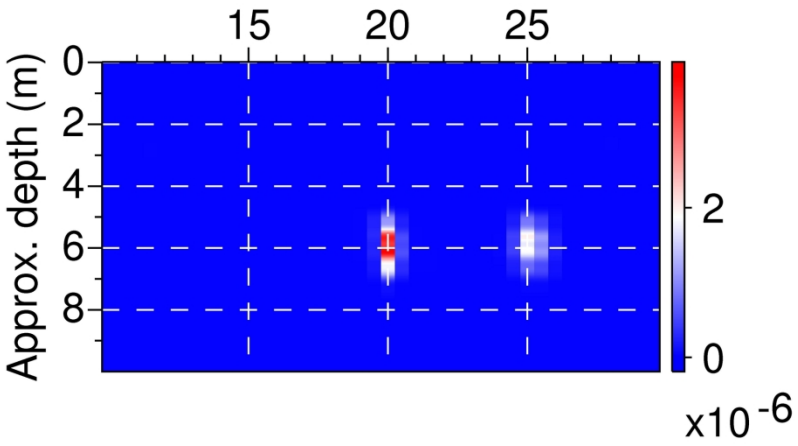


Figure 8d: Comparison of results from diffraction imaging by different approaches. (a),(b),(c) diffraction imaging of the data after Love-wave suppression by $f-k$ filtering, SI+AS, and SI+AS+SVI, respectively. Every second common-source gather is used. Phase-weighted stack (PWS) is applied to enhance the coherent summation of weak diffraction signals. (d),(e),(f) Similar to (a), (b), (c), but using all the modeled common-source gathers. (g), (h), (i) Similar to (d), (e), (f), but ordinary, linear stack is used to stack the weak diffraction signals.

204x122mm (300 x 300 DPI)

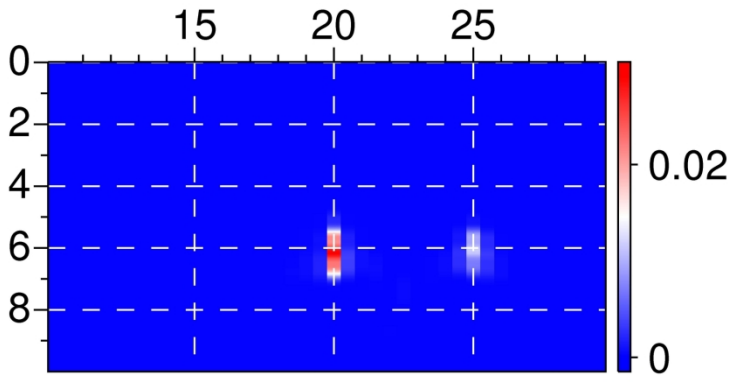


Figure 8e: Comparison of results from diffraction imaging by different approaches. (a),(b),(c) diffraction imaging of the data after Love-wave suppression by $f-k$ filtering, SI+AS, and SI+AS+SVI, respectively. Every second common-source gather is used. Phase-weighted stack (PWS) is applied to enhance the coherent summation of weak diffraction signals. (d),(e),(f) Similar to (a), (b), (c), but using all the modeled common-source gathers. (g), (h), (i) Similar to (d), (e), (f), but ordinary, linear stack is used to stack the weak diffraction signals.

204x122mm (300 x 300 DPI)

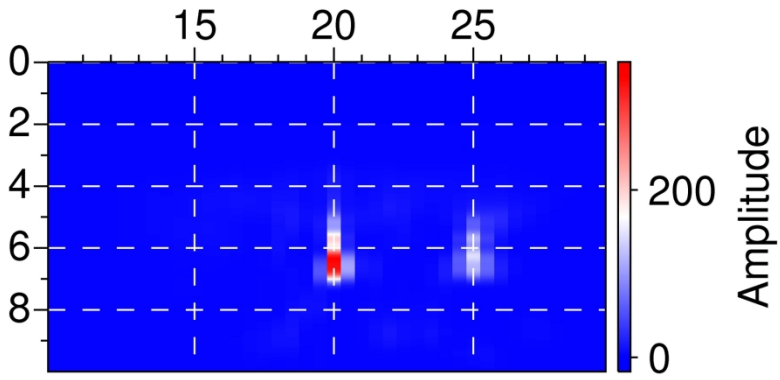


Figure 8f: Comparison of results from diffraction imaging by different approaches. (a),(b),(c) diffraction imaging of the data after Love-wave suppression by $f-k$ filtering, SI+AS, and SI+AS+SVI, respectively. Every second common-source gather is used. Phase-weighted stack (PWS) is applied to enhance the coherent summation of weak diffraction signals. (d),(e),(f) Similar to (a), (b), (c), but using all the modeled common-source gathers. (g), (h), (i) Similar to (d), (e), (f), but ordinary, linear stack is used to stack the weak diffraction signals.

204x122mm (300 x 300 DPI)

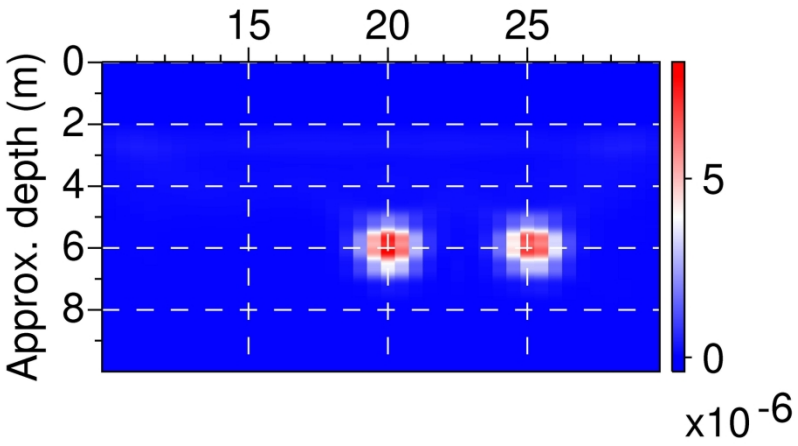


Figure 8g: Comparison of results from diffraction imaging by different approaches. (a),(b),(c) diffraction imaging of the data after Love-wave suppression by $f-k$ filtering, SI+AS, and SI+AS+SVI, respectively. Every second common-source gather is used. Phase-weighted stack (PWS) is applied to enhance the coherent summation of weak diffraction signals. (d),(e),(f) Similar to (a), (b), (c), but using all the modeled common-source gathers. (g), (h), (i) Similar to (d), (e), (f), but ordinary, linear stack is used to stack the weak diffraction signals.

204x122mm (300 x 300 DPI)

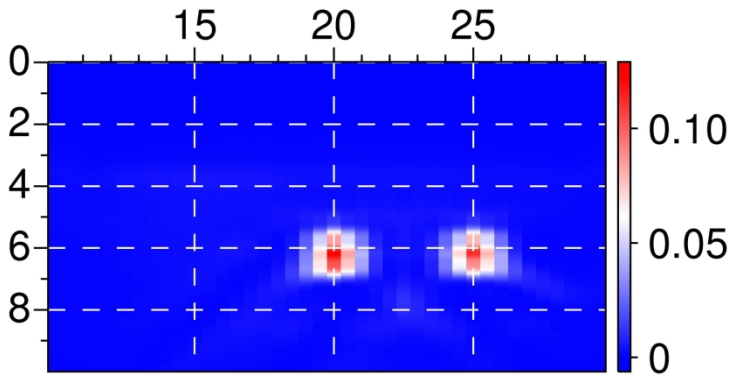


Figure 8h: Comparison of results from diffraction imaging by different approaches. (a),(b),(c) diffraction imaging of the data after Love-wave suppression by $f-k$ filtering, SI+AS, and SI+AS+SVI, respectively. Every second common-source gather is used. Phase-weighted stack (PWS) is applied to enhance the coherent summation of weak diffraction signals. (d),(e),(f) Similar to (a), (b), (c), but using all the modeled common-source gathers. (g), (h), (i) Similar to (d), (e), (f), but ordinary, linear stack is used to stack the weak diffraction signals.

204x122mm (300 x 300 DPI)

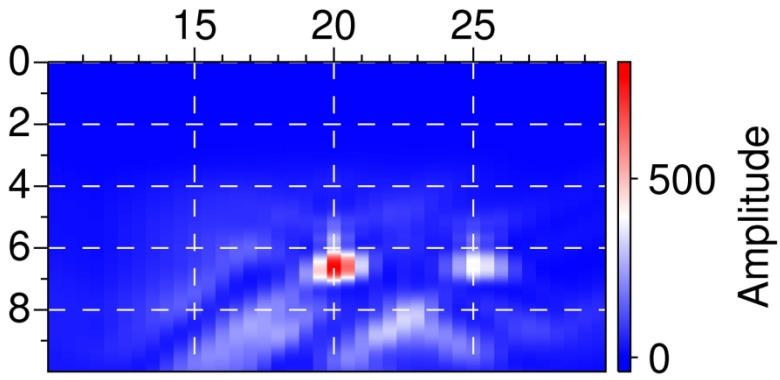


Figure 8i: Comparison of results from diffraction imaging by different approaches. (a),(b),(c) diffraction imaging of the data after Love-wave suppression by $f-k$ filtering, SI+AS, and SI+AS+SVI, respectively. Every second common-source gather is used. Phase-weighted stack (PWS) is applied to enhance the coherent summation of weak diffraction signals. (d),(e),(f) Similar to (a), (b), (c), but using all the modeled common-source gathers. (g), (h), (i) Similar to (d), (e), (f), but ordinary, linear stack is used to stack the weak diffraction signals.

204x122mm (300 x 300 DPI)

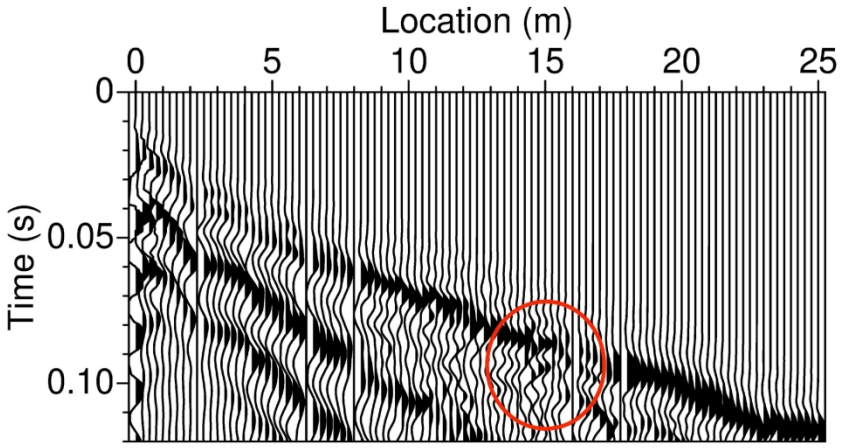


Figure 9a: (a) A typical preprocessed SH-wave shot gather from the field data acquired using a sledge-hammer source. The gather is dominated by strong Love waves. (c) Result after Love-wave suppression by SI+AS; (e) result after diffraction enhancement by SVI; (b),(d),(f) are the same as (a),(c),(e), but using S-wave vibrator as the source. The first 101 traces are displayed.

182x112mm (300 x 300 DPI)

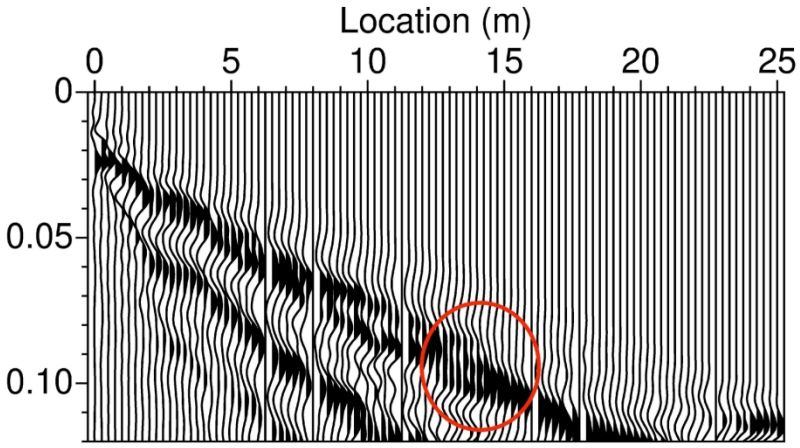


Figure 9b: (a) A typical preprocessed SH-wave shot gather from the field data acquired using a sledge-hammer source. The gather is dominated by strong Love waves. (c) Result after Love-wave suppression by SI+AS; (e) result after diffraction enhancement by SVI; (b),(d),(f) are the same as (a),(c),(e), but using S-wave vibrator as the source. The first 101 traces are displayed.

182x112mm (300 x 300 DPI)

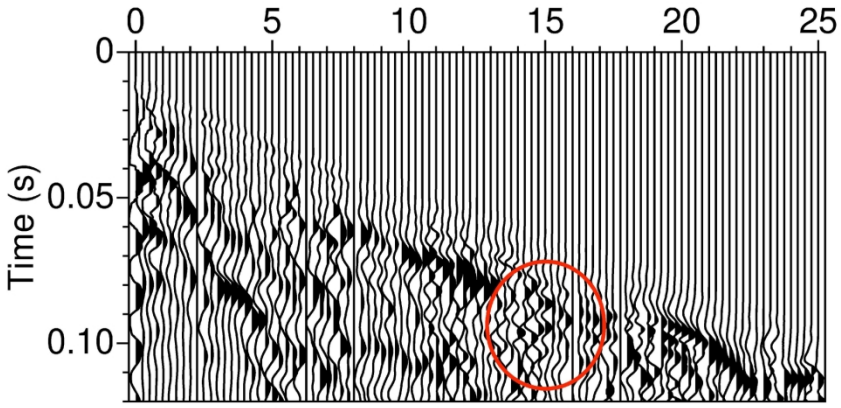


Figure 9c: (a) A typical preprocessed SH-wave shot gather from the field data acquired using a sledge-hammer source. The gather is dominated by strong Love waves. (c) Result after Love-wave suppression by SI+AS; (e) result after diffraction enhancement by SVI; (b),(d),(f) are the same as (a),(c),(e), but using S-wave vibrator as the source. The first 101 traces are displayed.

182x112mm (300 x 300 DPI)

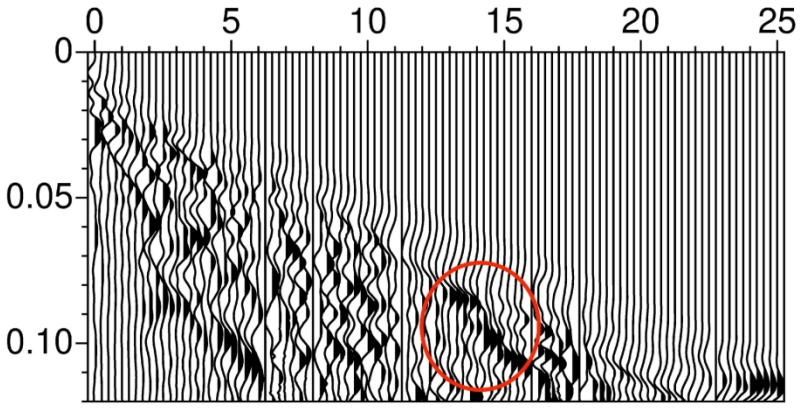


Figure 9d: (a) A typical preprocessed SH-wave shot gather from the field data acquired using a sledge-hammer source. The gather is dominated by strong Love waves. (c) Result after Love-wave suppression by SI+AS; (e) result after diffraction enhancement by SVI; (b),(d),(f) are the same as (a),(c),(e), but using S-wave vibrator as the source. The first 101 traces are displayed.

182x112mm (300 x 300 DPI)

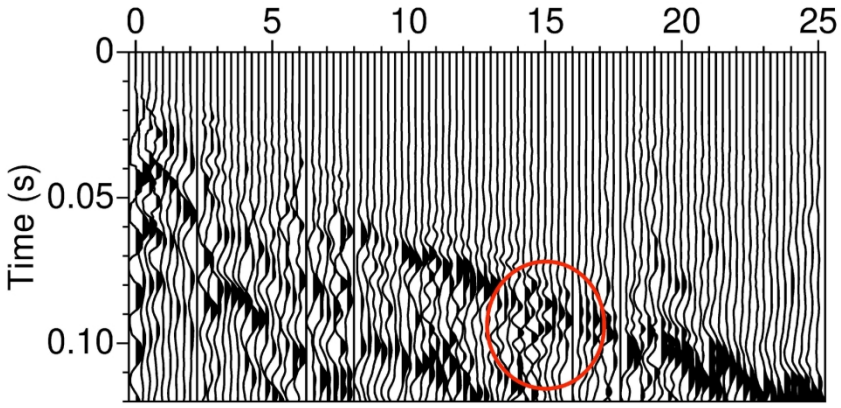


Figure 9e: (a) A typical preprocessed SH-wave shot gather from the field data acquired using a sledge-hammer source. The gather is dominated by strong Love waves. (c) Result after Love-wave suppression by SI+AS; (e) result after diffraction enhancement by SVI; (b),(d),(f) are the same as (a),(c),(e), but using S-wave vibrator as the source. The first 101 traces are displayed.

182x112mm (300 x 300 DPI)

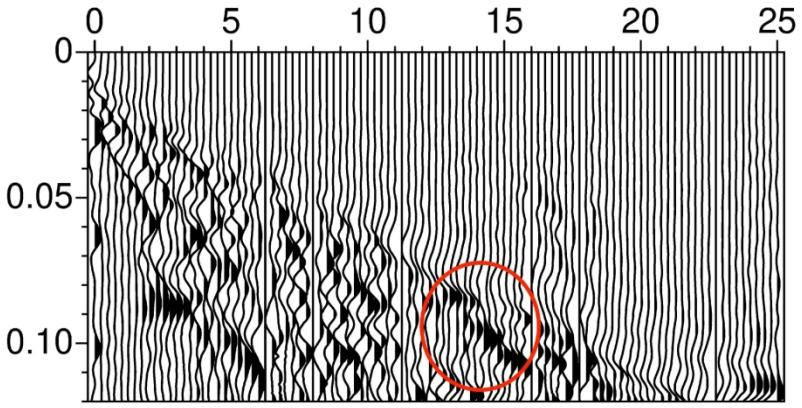


Figure 9f: (a) A typical preprocessed SH-wave shot gather from the field data acquired using a sledge-hammer source. The gather is dominated by strong Love waves. (c) Result after Love-wave suppression by SI+AS; (e) result after diffraction enhancement by SVI; (b),(d),(f) are the same as (a),(c),(e), but using S-wave vibrator as the source. The first 101 traces are displayed.

182x112mm (300 x 300 DPI)

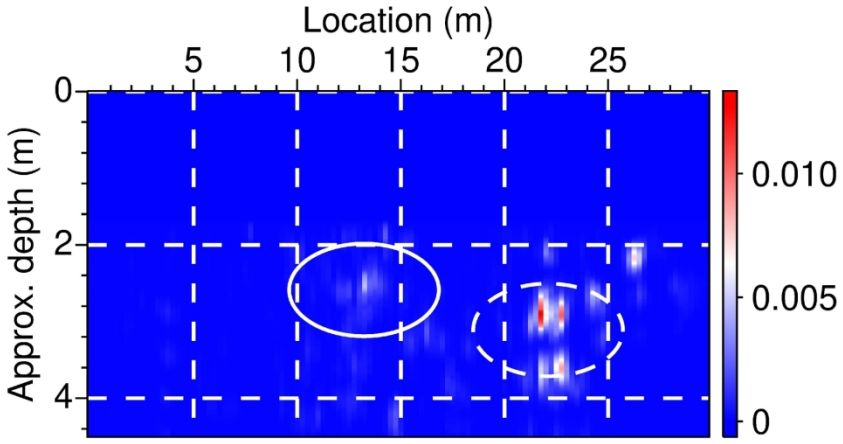


Figure 10a: Diffraction imaging result obtained from the field seismic data following our proposed workflow 1: (a) sledge-hammer data after Love-wave suppression by SI+AS; (b) sledge-hammer data after Love-wave suppression by SI+AS and diffraction enhancement by SVI; (c), (d) are same as (a), (b) but using S-wave vibrator data. High-amplitude anomalies (solid and dashed ellipses) indicate the potential locations of subsurface diffractor-like objects.

183x112mm (300 x 300 DPI)

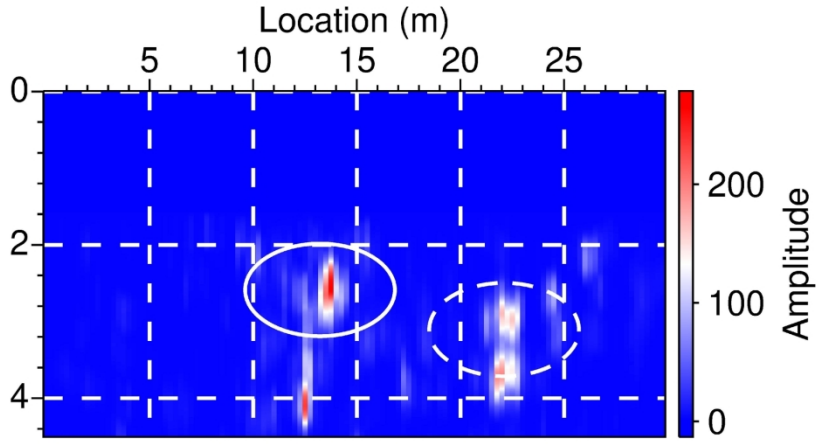


Figure 10b: Diffraction imaging result obtained from the field seismic data following our proposed workflow 1: (a) sledge-hammer data after Love-wave suppression by SI+AS; (b) sledge-hammer data after Love-wave suppression by SI+AS and diffraction enhancement by SVI; (c), (d) are same as (a), (b) but using S-wave vibrator data. High-amplitude anomalies (solid and dashed ellipses) indicate the potential locations of subsurface diffractor-like objects.

183x112mm (300 x 300 DPI)

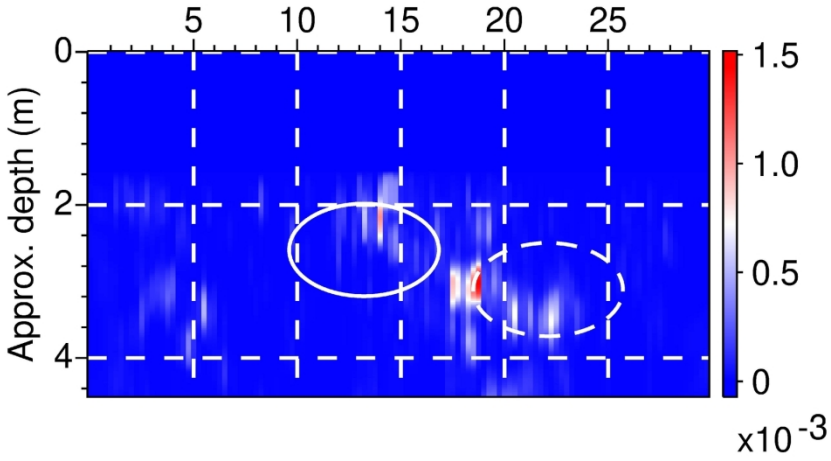


Figure 10c: Diffraction imaging result obtained from the field seismic data following our proposed workflow 1: (a) sledge-hammer data after Love-wave suppression by SI+AS; (b) sledge-hammer data after Love-wave suppression by SI+AS and diffraction enhancement by SVI; (c), (d) are same as (a), (b) but using S-wave vibrator data. High-amplitude anomalies (solid and dashed ellipses) indicate the potential locations of subsurface diffractor-like objects.

183x112mm (300 x 300 DPI)

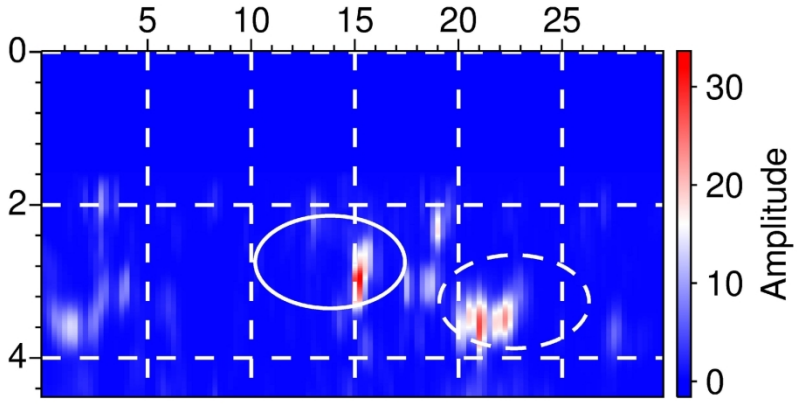


Figure 10d: Diffraction imaging result obtained from the field seismic data following our proposed workflow 1: (a) sledge-hammer data after Love-wave suppression by SI+AS; (b) sledge-hammer data after Love-wave suppression by SI+AS and diffraction enhancement by SVI; (c), (d) are same as (a), (b) but using S-wave vibrator data. High-amplitude anomalies (solid and dashed ellipses) indicate the potential locations of subsurface diffractor-like objects.

183x112mm (300 x 300 DPI)

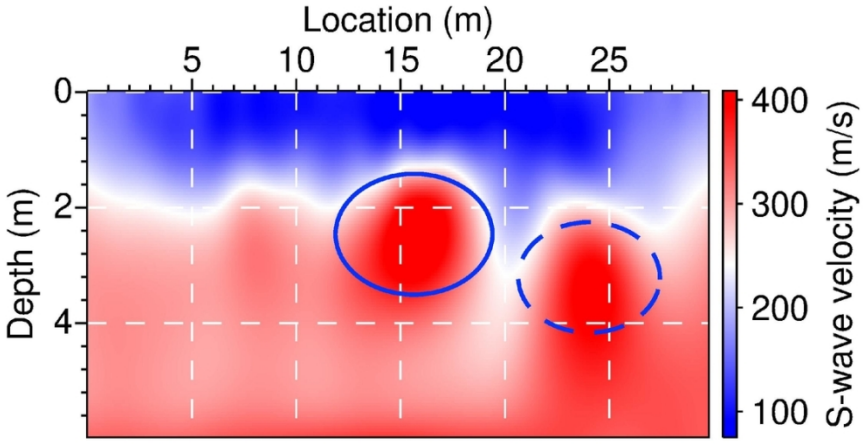


Figure 11: Two-dimensional subsurface V_S model obtained by elastic full-waveform inversion of the sledge-hammer data.

110x67mm (300 x 300 DPI)

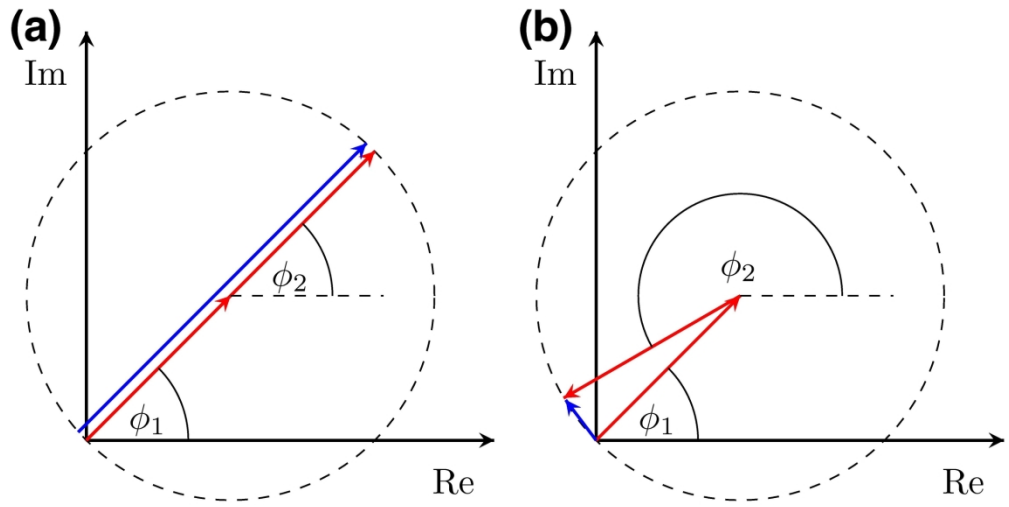


Figure B-1: Illustrations of the summation of $exp[i\phi_{1}(t)]$ and $exp[i\phi_{2}(t)]$ in the complex plane. Red arrows denote these two vectors, while the blue vector is the addition of these two vectors. (a) When two signals have the same instantaneous phase ($\phi_{1}(t) = \phi_{2}(t)$), the amplitude of the phase sum (blue arrow) will be 2, and the corresponding value of $c(t)$ will be 1. (b) When two signals have significantly different instantaneous phases, the amplitude of the phase sum (blue arrow) and the corresponding value of $c(t)$ will be approximately 0. Modified from Schimmel and Paulssen (1997).

202x117mm (300 x 300 DPI)